Supplementary Information for

Effects of non-fused and fused substituents in quinoxaline-based central units on conformation, aggregation, and photovoltaic properties of non-fused ring electron acceptors

Kenta Yamada,[a] Wataru Suzuki,[a] Motohisa Kubota,[b] Junichi Inamoto,[a] Mizuho Kondo,[a] Tomoyuki Koganezawa,[c] Yuki Chiga,[d] Ryo Takahata,[d,e] Toshiharu Teranishi,[d,e] Hiroshi Imahori[b,f,g] and Tomokazu Umeyama*[a]

[a.] Department of Applied Chemistry, Graduate School of Engineering, University of Hyogo, Himeji, Hyogo 671-2280, Japan.
[b.] Department of Molecular Engineering, Graduate School of Engineering, Kyoto University, Kyoto 615-8510, Japan
[c.] Japan Synchrotron Radiation Research Institute, 1-1-1, Kouto, Sayo-cho, Sayo-gun, Hyogo 679-5198, Japan
[d.] Institute for Chemical Research, Kyoto University, Gokasho, Uji 611-0011, Japan
[e.] Graduate School of Science, Kyoto University, Gokasho, Uji 611-0011, Japan
[f.] Institute for Integrated Cell-Material Sciences (WPI-iCeMS), Kyoto University, Nishikyo-ku, Kyoto 615-8510, Japan
[g.] Institute for Liberal Arts and Sciences (ILAS), Kyoto University, Kyoto 606-8316, Japan

E-mail: umeyama@eng.u-hyogo.ac.jp

List of Contents

1. Instruments

^{1}H NMR (400 MHz) and ^{13}C NMR (100 MHz) spectra were measured with a JEOL JNM-ECZ400R FT-NMR spectrometer at 293K. Chemical shifts (δ) for ^{1}H NMR are given in parts per million (ppm) referenced to the solvent peak (7.26 ppm for $CDCl_3$ and 7.02 ppm for 2-proton of C_6D_5Cl) as the internal standard. The chemical shifts for ^{13}C NMR were recorded in ppm downfield using the central peak of $CDCl_3$ (77.16 ppm) as the internal standard. Abbreviations used are s (singlet), d (doublet), t (triplet), q (quartet), and m (multiplet). Delay time, pulse width, acquisition time, number of scans, and spectral width for ^{1}H NMR measurements were 5 s, 6.52 μs, 2.732 s, 8 times, and 15 ppm. High-resolution mass spectra were measured on a LTQ Orbitrap XL (APCI, Thermo Fisher Scientific). Attenuated total reflectance (ATR) FT-IR spectra were recorded on a JASCO FT/IR-4600. Thermogravimetric analysis (TGA) measurements were conducted with a Shimadzu DTG-60 under flowing nitrogen at a scan rate of 10°C min^{-1}. Differential scanning calorimetry (DSC) analysis was made on a DSC7020 (Hitachi High technologies) at a scan rate of 10°C min^{-1}. UV–vis–near infrared (NIR) absorption spectra were obtained on an Agilent Cary 8454. Vis-NIR absorption measurements at low temperature was performed using UH5700 spectrophotometer (Hitachi High-Tech Science) equipped with cryostat CoolSpeK (UNISOKU). Steady-state fluorescence spectra were recorded on a JASCO FP-8650. Photoemission yield spectroscopy in air (PYSA) measurements were performed using an AC-3 (Riken Keiki). Time-correlated single photon counting (TCSPC) measurements using a HORIBA NanoLOG-TCSPC were conducted for fluorescence lifetime measurements on the nanosecond time-scale. The time resolution was ca. 200 ps. Atomic force microscopy (AFM) analyses were carried out with an Scanning Probe Microscope: NanoNaviReal (Hitachi High-Tech Science).

Photocurrent–voltage characteristics were measured with Keithley 2400 SourceMeter under a nitrogen atmosphere and simulated solar light (100 mW cm^{-2}, AM1.5) with OTENTO-SUN III solar simulator (Bunkoukeiki). Photocurrent action spectra were recorded with CEP-2000RR (Bunkoukeiki). Current–voltage characteristics of the electron- and hole-only devices for space charge-limited current (SCLC) measurements were conducted using Keithley 2400 SourceMeter under a nitrogen atmosphere.

2. Theoretical calculations

Optimized structures, thermodynamic stabilities, and molecular orbital distributions were theoretically estimated using density functional theory (DFT) at the B3LYP/6-31G(d) level. The Gaussian 16 program[S1] was used for all calculations. All structures were fully optimized without any symmetry restriction.

3. Measurements

SCLC. Single-carrier devices with configurations of ITO/PEDOT:PSS (40 nm)/active layer/MoO_3 (10 nm)/Ag and ITO/ZnO (30 nm)/active layer/PDINN/Ag were fabricated to measure hole and electron mobilities, respectively, of the blend films. The precursor for ZnO[S2] was prepared by dissolving zinc acetate dihydrate (0.5 g) into methanol (10 mL) under vigorous stirring for 0.5 h in air. 40 μL of the precursor for ZnO was spin-coated on top of the ITO-glass substrate at 3500 rpm for 40 s, followed by a thermal annealing in air at 200 ℃ for 15 min. The film thicknesses of ZnO were approximately 30 nm. Then, these substrates were transferred into a glove box filled with dried Ar gas to coat the active layer. The active layers were fabricated in a similar manner to those in OPV devices. The thickness was approximately 90–100 nm as measured by Dektak XT profilometer.

The mobility μ was derived by taking current–voltage curves and fitting the results to a space charge limited form, where the SCLC is described by:

$$J = 9\varepsilon_0\varepsilon_r\mu V^2/8L^3$$

where ε_0 is the permittivity of free space, ε_r is the dielectric constant of the polymer, μ is the charge mobility, V is the voltage drop across the device, and L is the thickness of the blend film. The dielectric constant ε_r is assumed to be 3, which is a typical value for organic semiconductors.

GIWAXS. Samples were prepared by spin-coating the NFREA, PBDB-T, or PBDB-T:NFREA solution on the glass substrate as conducted in the OPV device fabrications. GIWAXS measurements

were conducted at the SPring-8 on beamline BL46XU and BL19B2. The sample was irradiated at a fixed incident angle on the order of 0.12° through a Huber diffractometer with X-ray energy of 12.398 keV (X-ray wavelength λ = 0.10002 nm), and the GIWAXS patterns were recorded with a 2D image detector (Pilatus 300 K) with the sample-to-detector distances of 173.8 mm.

OPV devices. OPV devices were fabricated with a conventional device configuration as ITO/PEDOT:PSS/active layer/PDINN/Ag. Devices were prepared on patterned indium tin oxide (ITO) substrates which were cleaned by ultra-sonication in deionized water, $CHCl_3$, acetone, and tetramethylammonium hydroxide aqueous solution for 15 min each, and then deionized water for 25 min, followed by 2-propanol and ethanol for 15 min each. They were subsequently dried under nitrogen flow, and treated in a UV–ozone cleaner for 25 min. PEDOT:PSS aqueous solution (100 μL) through a 0.45-μm filter was spin-coated on substrates at 4000 rpm for 40 s. The PEDOT:PSS layer was dried at 220℃ for 10 min, and then transferred into a glove box filled with dried Ar gas to coat the active layer. A photoactive layer (PBDB-T:CRIC and PBDB-T:BRIC) was fabricated according to the following procedure. A blend solution of PBDB-T and CRIC (D:A = 1:1 by weight, 21 mg mL^{-1} in total) was prepared by dissolving in chlorobenzene (CB) with 1-chloronaphthalene (CN) (0.20%, v/v) as a solvent additive and stirred on a hotplate at 40°C 400 rpm for 3 h. A blend solution of PBDB-T and BRIC (D:A = 1:1.1 by weight, 20 mg/mL in total) was prepared by dissolving in CB with CN (0.40%, v/v) additive. Then, the mixed solutions were stirred on a hotplate at 40℃, 400 rpm for 3 h. A photoactive layer of PBDB-T:CRIC was spin-coated at 2500 rpm for 30 s on the top of the PEDOT:PSS layer, and annealed at 130℃ for 10 min. A photoactive layer of PBDB-T:BRIC was spin-coated at 3000 rpm for 30 s on the top of the PEDOT:PSS layer, and annealed at 130℃ for 10 min. The thickness of the photoactive layer was ca. 100 nm. Finally, to provide a PDINN cathode buffer layer, PDINN (1 mg mL^{-1} in methanol) was spin-coated at 3000 rpm for 30 s on the active layer, followed by the deposition of 100 nm Ag cathode under a high vacuum (< 2 $\times 10^{-4}$ Pa). All the active

device areas were 0.09 cm^2 through a shadow mask. The current density–voltage (*J–V*) curves were measured using Keithley 2400 source meter under 1 Sun (AM 1.5 G spectrum).

Contact angles. The contact angle tests were performed on a DSA100S - Drop Shape Analyzer. The surface energy of the polymers was characterized and calculated by the contact angles of the two probe liquids with the Wu model.[S3]

$$\frac{4\gamma^{d}_{water}\gamma^{d}}{\gamma^{d}_{water}+\gamma^{d}} + \frac{4\gamma^{p}_{water}\gamma^{p}}{\gamma^{p}_{water}+\gamma^{p}} = \gamma_{water}(1+\cos\theta_{water})$$

$$\frac{4\gamma^{d}_{oil}\gamma^{d}}{\gamma^{d}_{oil}+\gamma^{d}} + \frac{4\gamma^{p}_{oil}\gamma^{p}}{\gamma^{p}_{oil}+\gamma^{p}} = \gamma_{oil}(1+\cos\theta_{oil})$$

where γ is the total surface energy of acceptors and polymers, and γ^{d} and γ^{p} are the dispersion and polar components of γ, and θ is the droplet contact angle between sample and probe liquid. The values of γ^{d}_{water}, γ^{p}_{water}, γ^{d}_{oil}, γ^{p}_{oil} could be found from the literature.[S3]

4. Materials

3,6-Dibromo-4,5-bis(2-ethylhexyloxy)-1,2-benzenediamine (compound 1),[S4] 4,4-diethylhexyl-4*H*-cyclopenta[2,1-*b*:3,4-*b*′]dithiophene-2-carbaldehyde (CPDT-CHO),[S5] and 5,6-difluoro-1,1-dicyanomethylene-3-indanone (IC-F)[S6] were synthesized according to the reported procedures. PBDB-T was purchased from 1-Material. PEDOT:PSS (Clevios P VP AI 4083) and PDINN were obtained from Ossila. All other chemicals were purchased from commercial supplier and used without further purification.

5. Synthesis

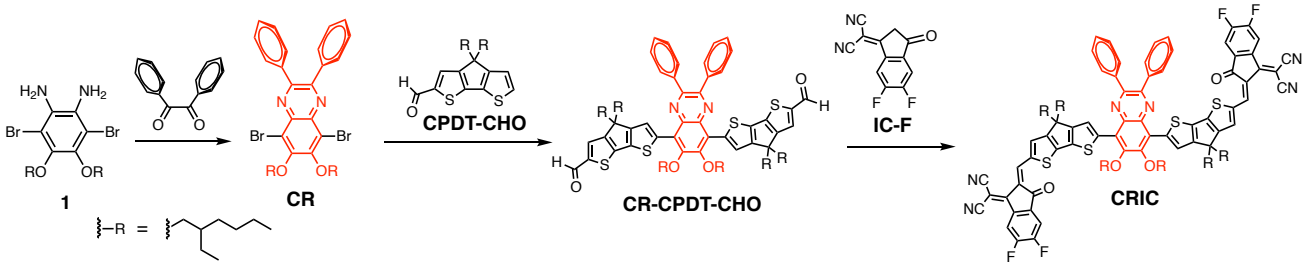

CR. A mixture of compound 1 (700 mg, 1.34 mmol) and benzil (0.382 g, 2.1 mmol) in acetic acid (50 mL) was heated to 80°C and stirred overnight. Then, the mixture was cooled to room temperature. Acetic acid was removed by extraction with CH_2Cl_2 and washed with water. The organic layer was dried over Na_2SO_4 and the residue was purified by column chromatography on silica gel with hexane/dichloromethane (1/1) as eluent to afford the product as yellow white solid in 88% yield. ^{1}H NMR (400 MHz, $CDCl_3$) δ (ppm): 7.63 (dd, J = 8.0, 1.0, 4H), 7.32-7.40 (m, 6H), 4.07 (d, J = 6.4 Hz, 4H), 0.84-1.93 (m, 30H). ^{13}C NMR (400 MHz, $CDCl_3$) δ (ppm): 154.20, 152.77, 138.33, 137.22, 130.34, 129.37, 128.43, 117.20, 40.72, 30.32, 29.27, 23.73, 23.27, 14.31, 11.30. HRMS (p APCI): calcd for $[C_{36}H_{44}Br_2N_2O_2+H]^+$: 695.1848; found: 695.1848. IR (ATR, cm^{-1}): ν_{max} 3007, 2990, 2958, 2928, 2871, 2859, 2707, 2695, 2383, 2367, 2349, 2328, 2316, 2309, 1460, 1425, 1349, 1275, 1261, 1195, 1092, 1070, 1028, 989, 955, 922, 897, 819, 755, 697, 647. Melting point: 60–64°C.

CR-CPDT-CHO. CR (178 mg, 0.26 mmol), CPDT-CHO (200 mg, 0.47 mmol), and trimethylacetic acid (39 mg, 0.38 mmol), Cs_2CO_3 (1.02 g, 3.1 mmol) were dissolved in dry *o*-xylene (12 mL) under nitrogen atmosphere. $Pd_2(dba)_3{\cdot}CHCl_3$ (40 mg, 0.04 mmol) and P(*o*-$CH_3OPh)_3$ (28 mg, 0.08 mmol) were added into reaction mixture and then the solution was heated at 120°C for 18 h. The crude product was extracted with dichloromethane, washed with water, and dried with anhydrous magnesium sulfate. After removing the solvent, the product was purified by silica gel column chromatography with the solvent mixture of hexane/dichloromethane (15/85) as the eluent, yielding red oil (269 mg, yield = 75%). ^{1}H NMR (400 MHz, $CDCl_3$) δ (ppm): 9.85 (s, 2H), 8.303 (s, 0.125H), 8.295 (s, 0.25H), 8.286 (s, 0.125H), 8.263 (s, 0.25H), 8.253 (s, 0.5H), 8.242 (s, 0.25H), 8.218 (s, 0.125H), 8.205 (s, 0.25H),

8.192 (s, 0.125H), 7.61-7.68 (m, 4H), 7.610 (s, 0.5H), 7.602 (s, 1H), 7.595 (s, 0.5H), 7.34-7.42 (m, 6H), 3.98-4.05 (m, 4H), 1.89-2.10 (m, 8H), 1.25-1.58 (m, 12H), 0.51-1.10 (m, 78H). ^{13}C NMR (400 MHz, $CDCl_3$) δ (ppm): 182.69, 161.71, 157.74, 153.36, 150.64, 150.56, 148.92, 142.99, 138.88, 138.67, 131.15, 130.45, 130.38, 129.00, 128.34, 126.50, 123.91, 78.25, 54.05, 54.00, 43.51, 43.44, 40.62, 35.67, 35.54, 34.35, 34.21, 30.52, 29.31, 28.73, 28.64, 27.58, 23.78, 23.33, 22.97, 22.85, 14.31, 14.24, 14.13, 11.26, 10.75. HRMS (p APCI): calcd for $[C_{88}H_{118}N_2O_4S_4]^+$: 1394.7974; found: 1394.7974. IR (ATR, cm^{-1}): ν_{max} 3007, 2989, 2956, 2921, 2870, 2856, 2708, 2693, 2384, 2362, 2348, 2341, 2327, 2316, 2308, 2300, 1649, 1497, 1459, 1422, 1395, 1377, 1366, 1339, 1276, 1261, 1223, 1178, 1160, 1139, 1132, 1093, 1070, 1029, 1012, 954, 917, 897, 859, 795, 755, 697, 652.

CRIC. To a flask was added CR-CPDT-CHO (212 mg, 0.15 mmol), IC-F (130 mg, 0.57 mmol) and dried $CHCl_3$ (15 mL). Then the mixture was frozen by liquid nitrogen. After vacuum and N_2 circulated for three times, pyridine (0.6 mL) was added. The mixture was refluxed at 70°C for 16 h. After removing the solvent, silica gel column chromatography was used to purify the product with the mixture of hexane and dichloromethane (15:85, v/v) as the eluent, yielding a blue solid (180 mg, 65%). ^{1}H NMR (400 MHz, $CDCl_3$) δ (ppm): 8.92 (s, 2H), 8.53 (dd, J = 10 Hz, 6.8 Hz, 2H), 8.445 (s, 0.125H), 8.438 (s, 0.25H), 8.432 (s, 0.125H), 8.42-8.39 (m, 1H), 8.384 (s, 0.125H), 8.374 (s, 0.25H), 8.363 (s, 0.125H), 7.61-7.74 (m, 8H), 7.39-7.43 (m, 6H), 4.05-4.10 (m, 4H), 1.89-2.10 (m, 8H), 1.25-1.58 (m, 12H), 0.51-1.10 (m, 78H). ^{13}C NMR (400 MHz, $CDCl_3$) δ (ppm): 186.37, 165.56, 160.42, 159.85, 158.74, 155.62, 155.49, 153.71, 153.03, 152.89, 151.20, 151.15, 143.68, 139.91, 139.09, 138.76, 138.39, 138.34, 138.29, 136.69, 136.61, 136.36, 134.51, 129.27, 128.53, 126.97, 124.19, 118.99, 115.03, 114.84, 112.49, 112.31, 78.67, 67.50, 53.88, 53.85, 43.59, 40.66, 35.77, 34.28, 34.15, 30.54, 29.83, 29.33, 28.70, 28.52, 27.57, 27.41, 23.85, 23.34, 23.00, 22.87, 14.21, 14.24, 14.12, 11.27, 10.78, 10.66. HRMS (p APCI): calcd for $[C_{112}H_{123}F_4N_6O_4S_4-H]^+$: 1818.8347; found: 1818.8357. IR (ATR, cm^{-1}): ν_{max} 3007 2989, 2918, 2858, 2850, 2707, 2693, 2415, 2383, 2366, 2347, 2340, 2327, 2316, 2308,

2300, 2214, 1689, 1604, 1540,1535, 1488, 1475, 1460, 1397, 1376, 1348, 1340, 1276, 1261, 1227, 1131, 1093, 1064, 1031, 992, 914, 896, 889, 819, 755, 725, 704, 672.

Although the compounds with the same structures with BR, BR-CPDT-CHO, and BRIC were already reported,[S7] detailed procedures are described below because the synthetic routes are different.

BR. A mixture of compound 1 (655 mg, 1.25 mmol) and phenanthraquinone (0.382 g, 2.1 mmol) in 50 mL acetic acid was heated to 80℃ and stirred overnight. After that, the mixture was cooled to room temperature. Acetic acid was removed by extraction with CH_2Cl_2 and washed with water. The organic layer was dried over Na_2SO_4 and the residue was purified by column chromatography on silica gel with hexane/dichloromethane (2/1) as eluent to afford the product as yellow solid in 77% yield. ^{1}H NMR (400 MHz, $CDCl_3$) δ (ppm): 9.48 (dd, J = 7.6 Hz, 1.2 Hz, 2H), 8.58 (d, J = 7.6 Hz, 2H), 7.76-7.85 (m, 4H), 4.14 (d, J = 6.4 Hz, 4H), 0.84-1.93 (m, 30H).

BR-CPDT-CHO. BR (220 mg, 0.31 mmol), CPDT-CHO (265 mg, 0.62 mmol), and trimethylacetic acid (39 mg, 0.38 mmol), Cs_2CO_3 (1.02 g, 3.1 mmol) were dissolved in dry *o*-xylene (12 mL) under nitrogen atmosphere. $Pd_2(dba)_3{\cdot}CHCl_3$ (40 mg, 0.04 mmol) and P(*o*-$CH_3OPh)_3$ (28 mg, 0.08 mmol) were added into reaction mixture and then the solution was heated at 120°C for 18 h. The crude product was extracted with dichloromethane, washed with water, and dried with anhydrous magnesium sulfate. After removing the solvent, the product was purified by silica gel column chromatography with the solvent mixture of hexane/dichloromethane (15/85) as the eluent, yielding red oil (336 mg, yield = 77%). ^{1}H NMR (400 MHz, $CDCl_3$) δ (ppm): 9.89 (s, 2H), 9.41 (d, J = 8.4 Hz, 0.5H), 9.38 (d, J = 7.6 Hz, 1H), 9.34 (d, J = 8.0 Hz, 0.5H), 8.64 (d, J = 8.4 Hz, 2H), 8.215 (s, 0.125H), 8.208 (s, 0.25H), 8.202 (s, 0.125H), 8.168 (s, 0.25H), 8.162 (s, 0.5H), 8.152 (s, 0.25H), 8.115 (s, 0.125H), 8.106 (s, 0.25H), 8.096 (s, 0.125H), 7.85 (dd, J = 7.6 Hz, 7,6 Hz, 2H), 7.78 (dd, J = 6.4 Hz, 6.4 Hz, 0.5H), 7.76 (dd, J =

7.0 Hz, 7.0 Hz, 1H), 7.74 (dd, *J* = 6.6 Hz, 6.6 Hz, 0.5H), 7.68 (s, 0.5H), 7.67 (s, 1H), 7.66 (s, 0.5H), 3.98-4.05 (m, 4H), 1.94-2.15 (m, 8H), 1.25-1.57 (m, 12H), 0.51-1.10 (m, 78H).

BRIC. To a flask was added BR-CPDT-CHO (336 mg, 0.24 mmol), IC-F (250 mg, 1 mmol) and dried $CHCl_3$ (20 mL). Then the mixture was frozen by liquid nitrogen. After vacuum and N_2 circulated for three times, pyridine (0.8 mL) was added. The mixture was refluxed at 70°C for 16 h. After removing the solvent, silica gel column chromatography was used to purify the product with the mixture of hexane and dichloromethane 15:85, v/v) as the eluent, yielding a blue solid (0.18 g, 42%). ^{1}H NMR (400 MHz, $CDCl_3$) δ (ppm): 9.40 (d, *J* = 8.4 Hz, 0.5H), 9.38 (d, *J* = 8.8 Hz, 1H), 9.35 (d, *J* = 7.6 Hz, 0.5H), 8.95 (s, 2H), 8.64 (d, *J* = 8.4 Hz, 2H), 8.67 (d, *J* = 8.4 Hz, 2H), 8.52 (dd, *J* = 10 Hz, 6.4 Hz, 2H), 8.351 (s, 0.125H), 8.346 (s, 0.25H), 8.340 (s, 0.125H), 8.28-8.32 (m, 1H), 8.269 (s, 0.125H), 8.261 (s, 0.25H), 8.253 (s, 0.125H), 7.80-7.91 (m, 4H), 7.70-7.80 (br, 2H), 7.68 (t, *J* = 7.6 Hz, 2H), 4.05-4.15 (m, 4H), 1.89-2.10 (m, 8H), 1.25-1.58 (m, 12H), 0.51-1.10 (m, 78H).

6. Supplementary notes

It is known that the β-protons of CPDT with 2-ethylhexyl groups exhibit a complex ^{1}H NMR spectral pattern.[S8] However, the cause of this complexity has not been investigated in detail so far. To address this, we synthesized C8-CPDT-CHO,[S9] in which two achiral linear octyl groups were introduced into CPDT, and measured its ^{1}H NMR spectrum (Fig. S3d). In contrast to the spectrum of CPDT-CHO with chiral 2-ethylhexyl groups (Fig. S3a), the β-proton of the thiophene ring bearing the CHO group appeared as a single singlet signal at 7.569 ppm, while the β-proton of the other thiophene ring appeared as a doublet signal centered at 6.973 ppm. These results clearly indicate that the ^{1}H NMR signals of the thiophene β-protons in CPDT derivatives are influenced by the two alkyl groups at the 4-position (Fig. S1a). Furthermore, in the ^{1}H NMR spectrum of CPDT-CHO (Fig. S3a), the complex

spectral patterns of the thiophene β-protons reflect the different chirality combinations of the two 2-ethylhexyl groups, specifically (*R*,*R*) : (*R*,*S*) and (*S*,*R*) : (*S*,*S*) = 1 : 2 : 1.

7. Supplementary figures and tables

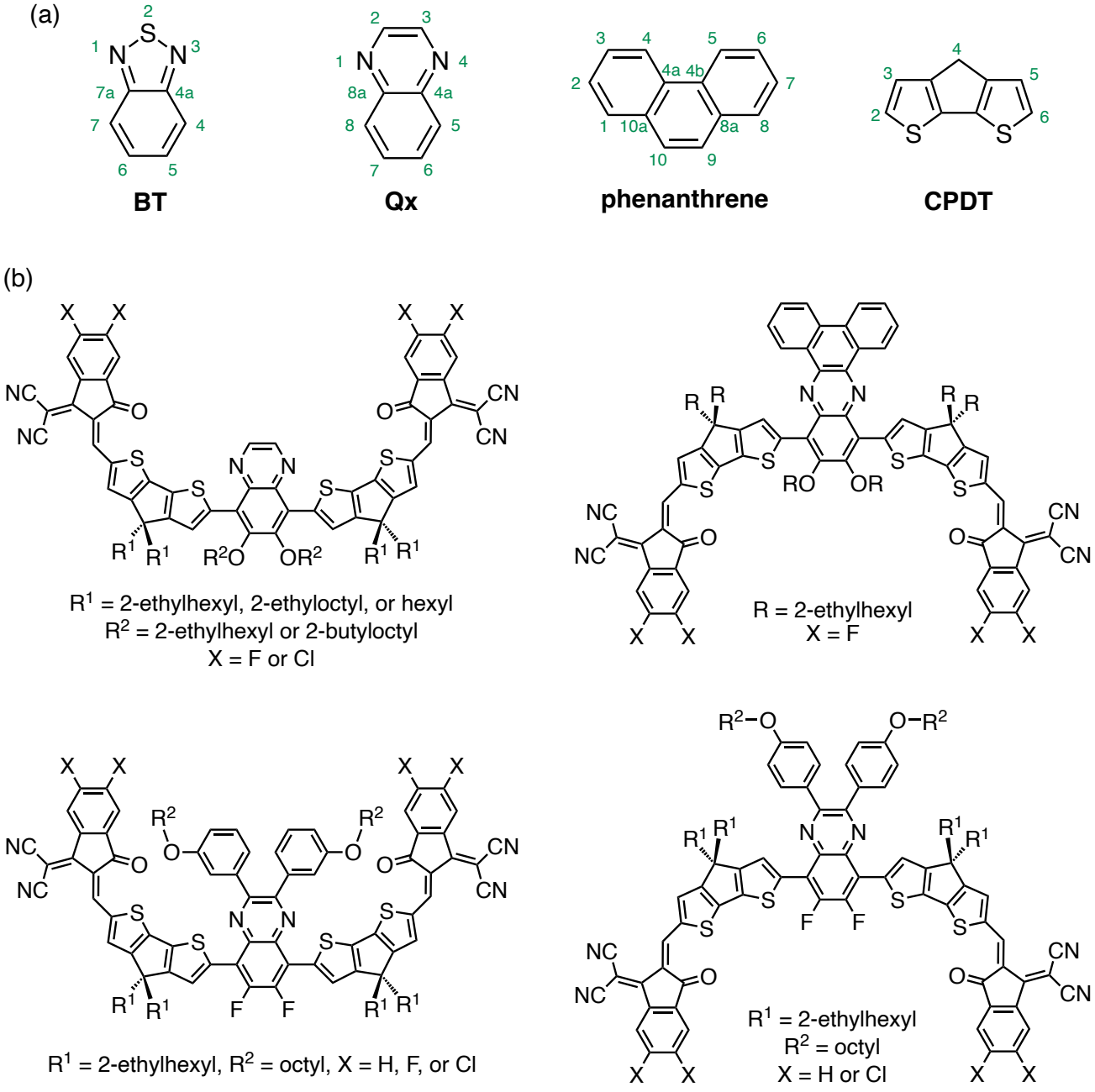

Fig. S1 (a) Structures of 2,1,3-benzothiadiazole (BT), quinoxaline (Qx), phenanthrene, and 4*H*-cyclopenta[1,2-*b*:5,4-*b*′]dithiophene (CPDT) with numbering (green). (b) Structures of previously reported Qx-based A−D−A'−D−A type NFREAs.[S10]-[S13]

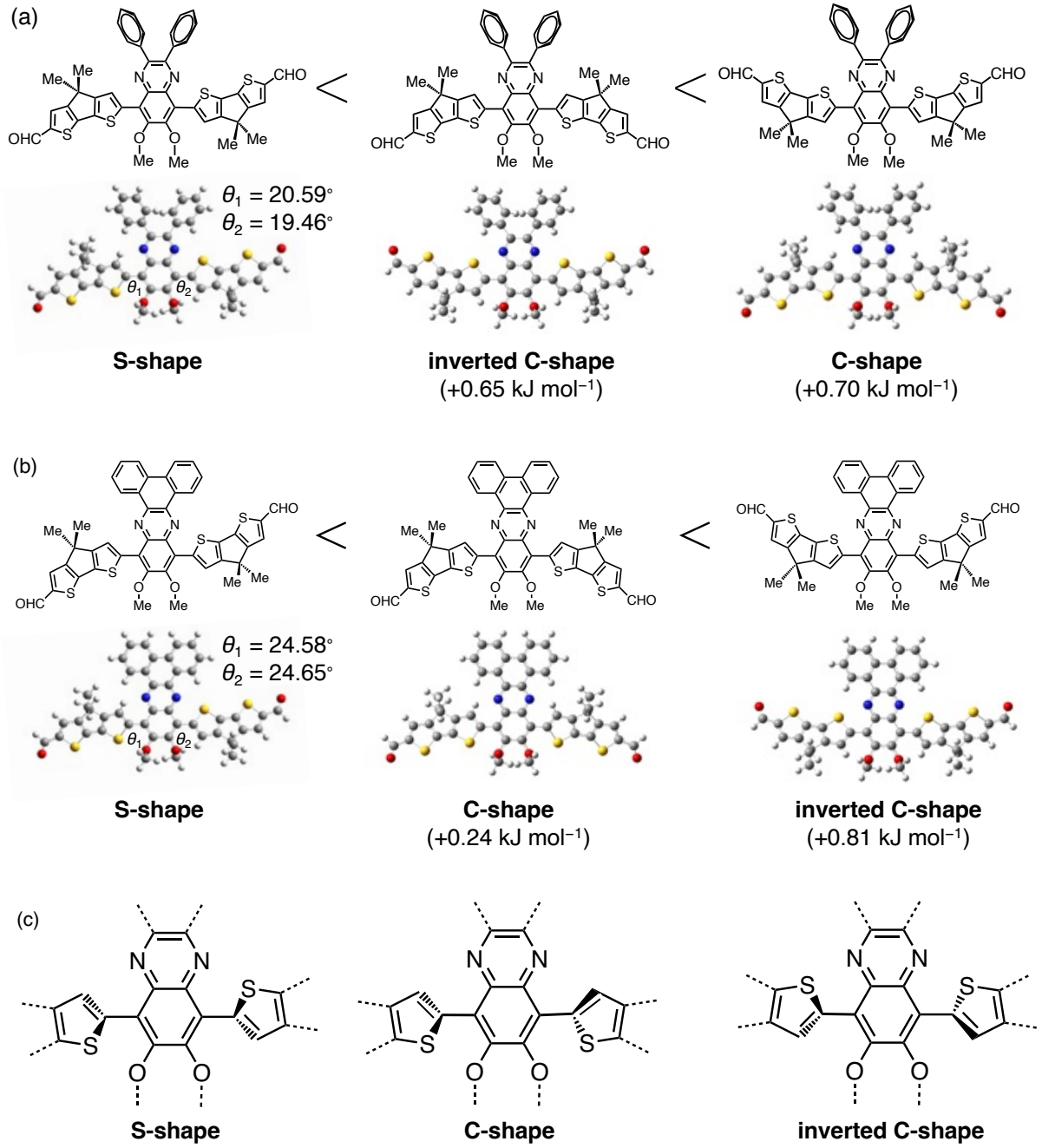

Fig. S2 Chemical structures and optimized geometries of S-, inverted C-, and C-shaped conformations for (a) CR-CPDT-CHO and (b) BR-CPDT-CHO models with methyl groups. The energies were calculated based on density functional theory (DFT) at the B3LYP/6-31G(d) level. The values in parentheses are energies relative to the S-shaped conformation. (c) Schematic structures around the A' core of CRIC and BRIC with S-, C-, and inverted C-shaped conformations.

(a)

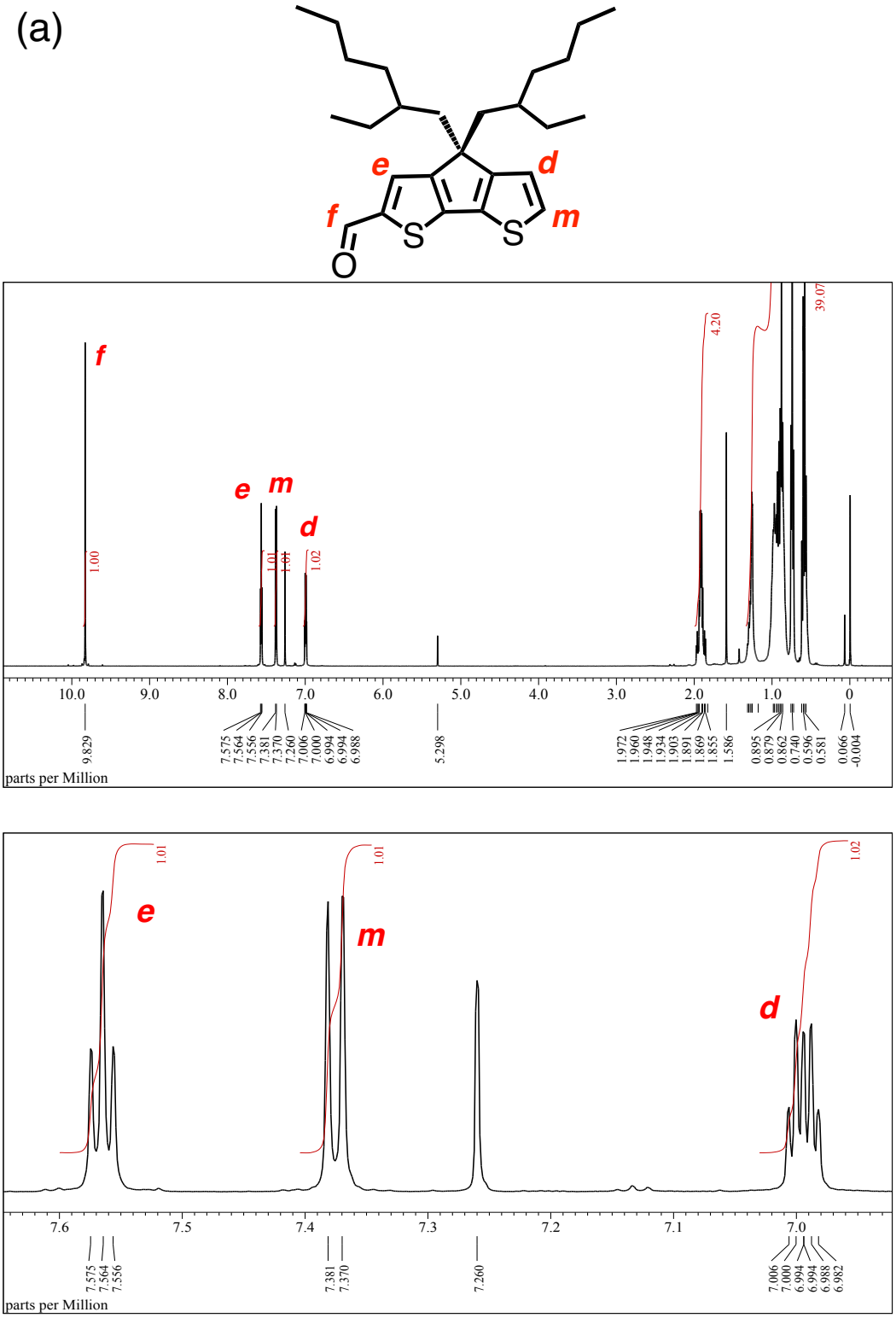
e
d
f
m
S
S
O
f
e
m
d
1.00
1.01
1.01
1.02
4.20
39.07
10.0
9.0
8.0
7.0
6.0
5.0
4.0
3.0
2.0
1.0
0
9.829
7.575
7.564
7.556
7.381
7.370
7.260
7.006
7.000
6.994
6.994
6.988
5.298
1.972
1.960
1.948
1.934
1.903
1.891
1.869
1.855
1.586
0.895
0.879
0.862
0.740
0.596
0.581
0.066
-0.004
parts per Million
1.01
1.01
1.02
e
m
d
7.6
7.5
7.4
7.3
7.2
7.1
7.0
7.575
7.564
7.556
7.381
7.370
7.260
7.006
7.000
6.994
6.994
6.988
6.982
parts per Million

(b)

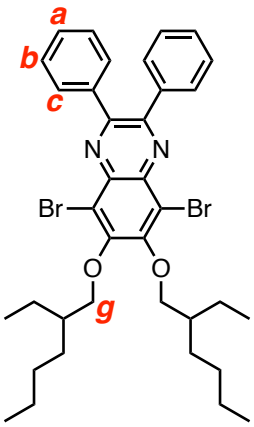
a
b
c
N
N
Br
Br
O
O
g

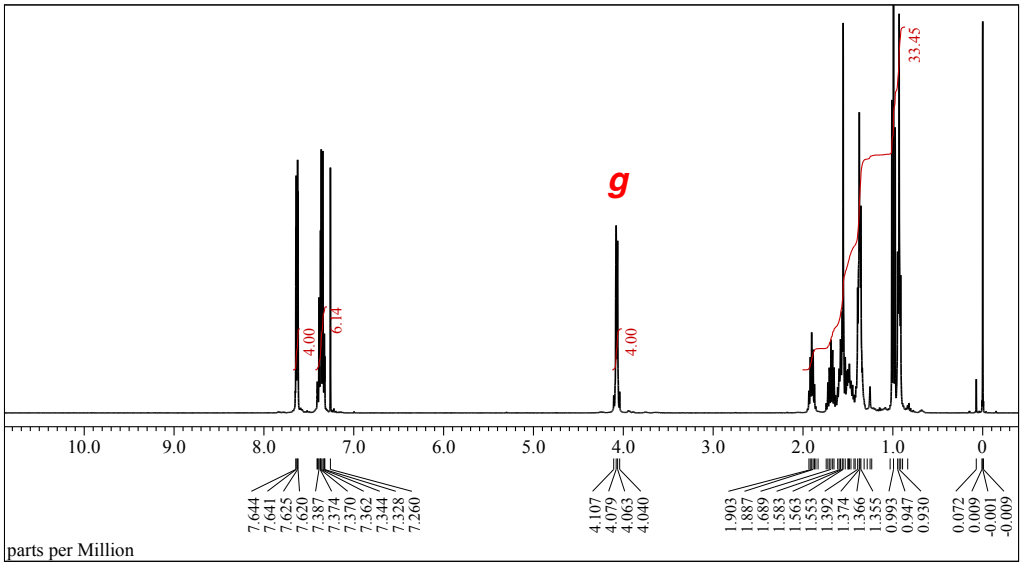
g
33.45
4.00
6.14
4.00
10.0
9.0
8.0
7.0
6.0
5.0
4.0
3.0
2.0
1.0
0
7.644
7.641
7.625
7.620
7.387
7.374
7.370
7.362
7.344
7.328
7.260
4.107
4.079
4.063
4.040
1.903
1.887
1.689
1.583
1.563
1.553
1.392
1.374
1.366
1.355
0.993
0.947
0.930
0.072
0.009
-0.001
-0.009
parts per Million

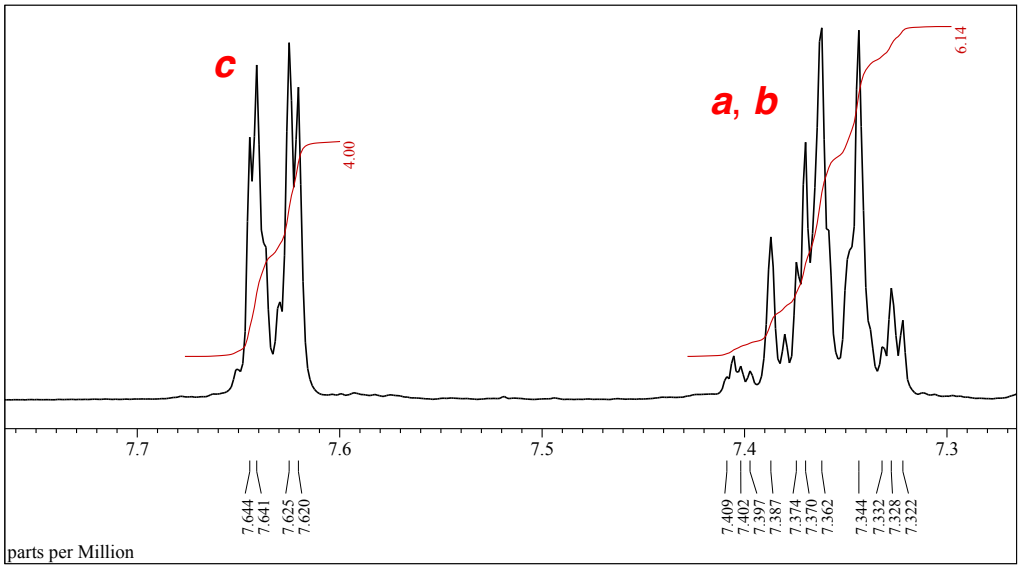
c
a, b
4.00
6.14
7.7
7.6
7.5
7.4
7.3
7.644
7.641
7.625
7.620
7.409
7.402
7.397
7.387
7.374
7.370
7.362
7.344
7.332
7.328
7.322
parts per Million

(c)

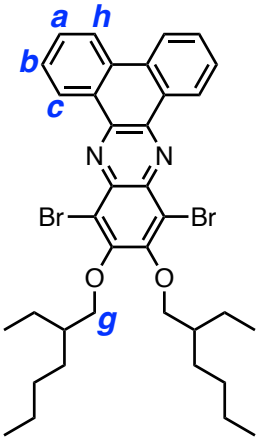
a
h
b
c
N
N
Br
Br
O
O
g

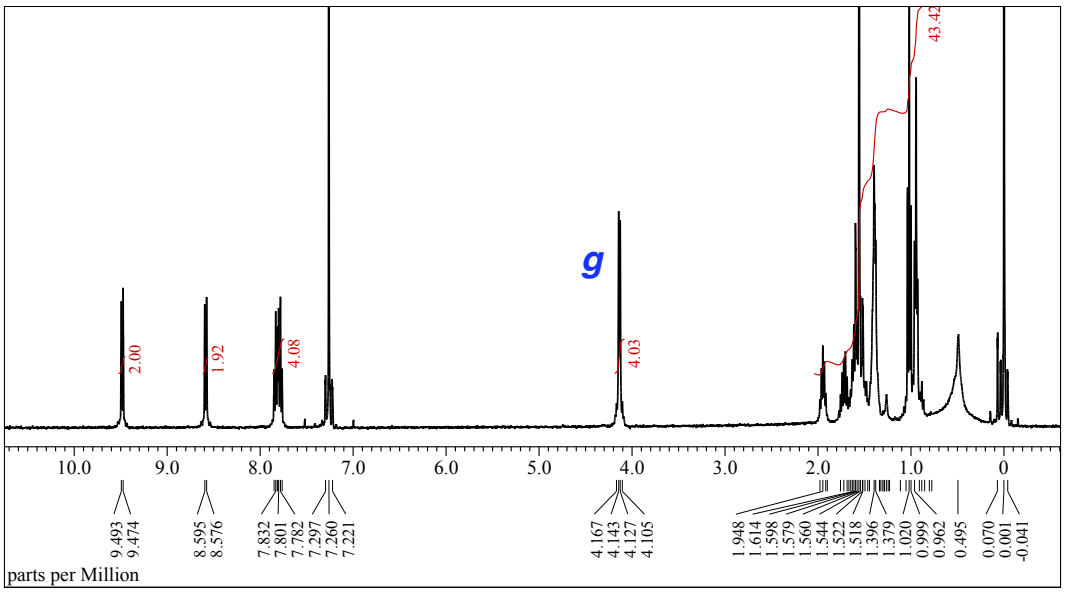
g
2.00
1.92
4.08
4.03
43.42
parts per Million

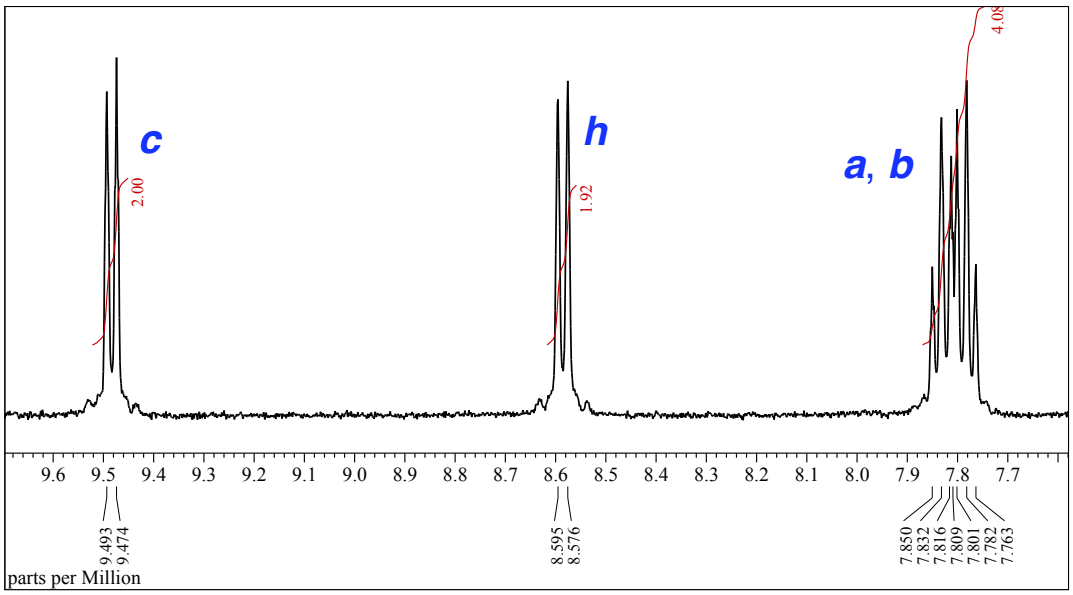
c
h
a, b
2.00
1.92
4.08
parts per Million

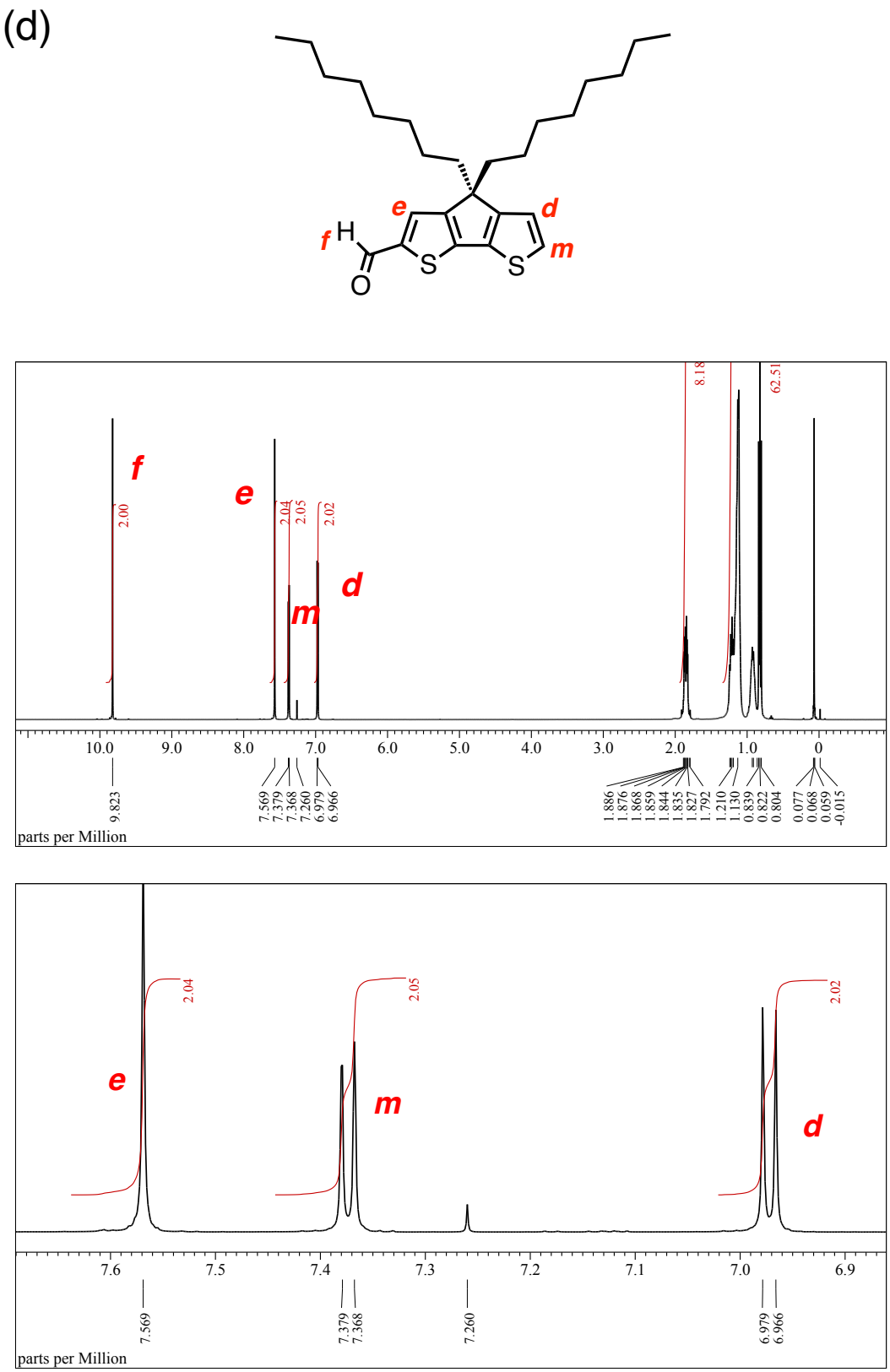

Fig. S3 ^{1}H NMR spectra of (a) CPDT-CHO, (b) CR, (c) BR, and (d) C8-CPDT-CHO in $CDCl_3$ with some peak assignments.

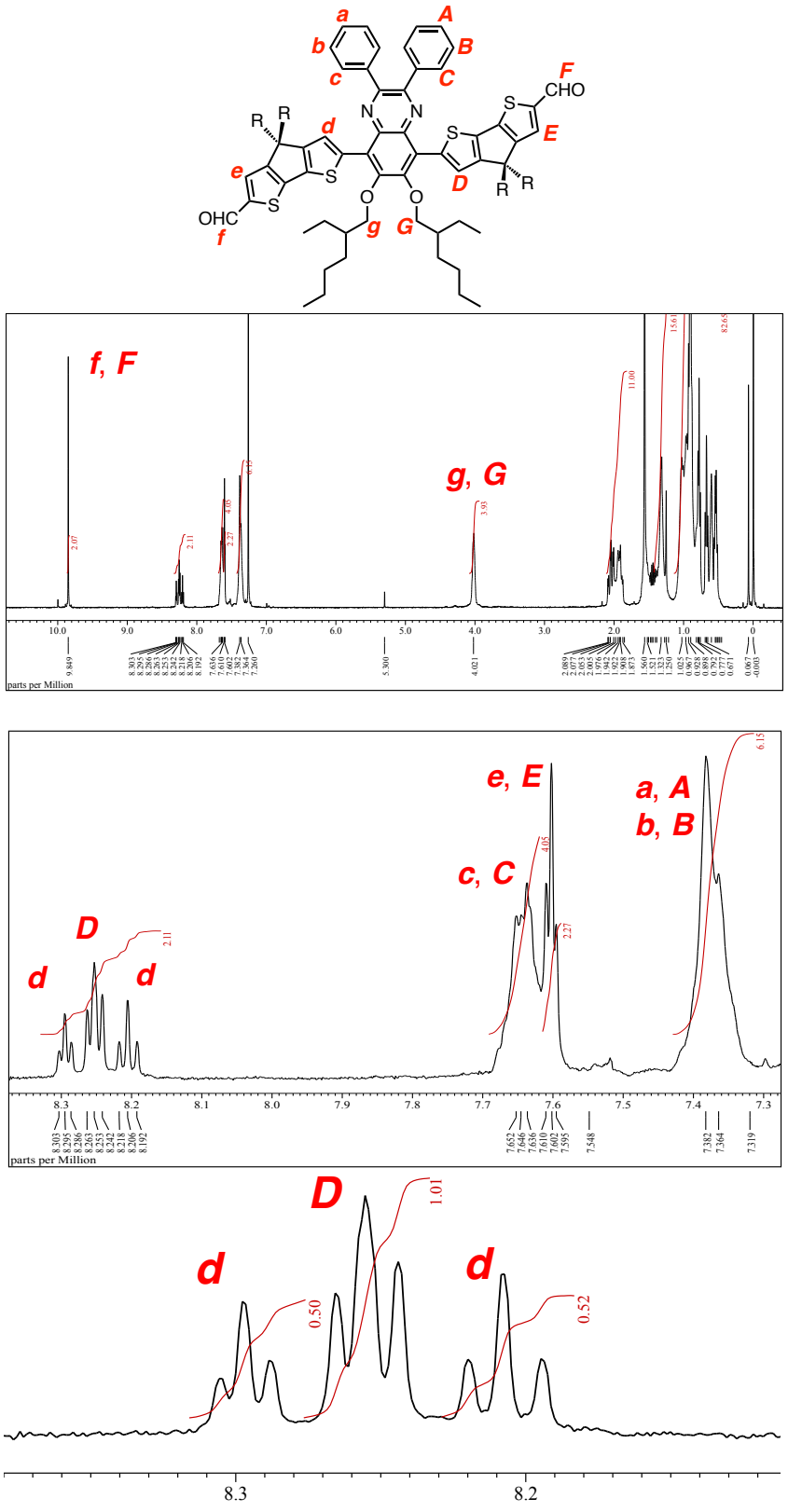

Fig. S4 ^{1}H NMR spectra of CR-CPDT-CHO in $CDCl_3$ with some peak assignments.

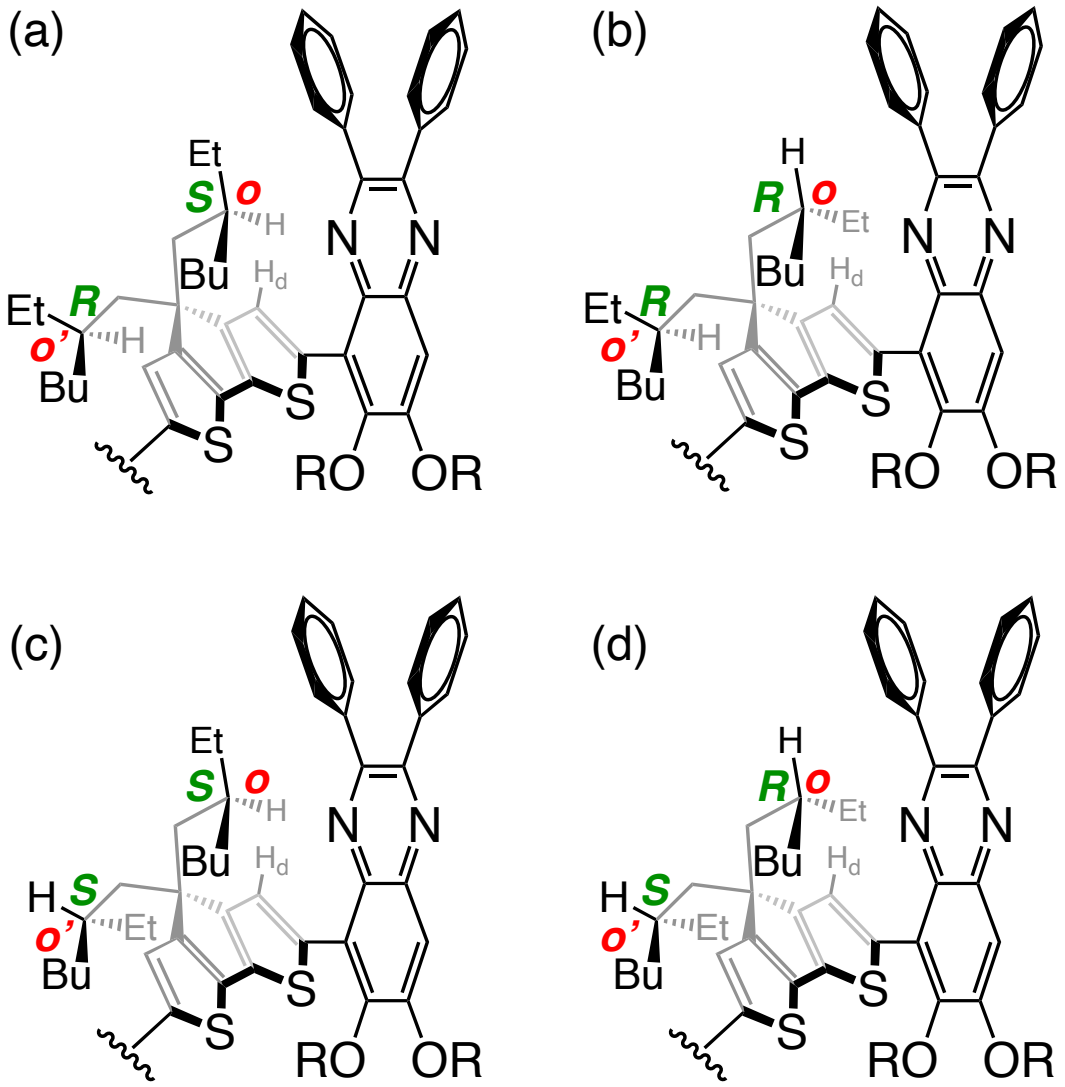

Fig. S5 Schematic images of steric repulsion between the (*R* or *S*)-2-ethylhexyl groups on CPDT and the CR core unit. Apparently, only one of the 2-ethylhexyl chains (the chain with ***o***) causes steric repulsion with the CR unit. Consequently, the steric repulsion in (a) and (c) is equivalent, as is the steric repulsion in (b) and (d).

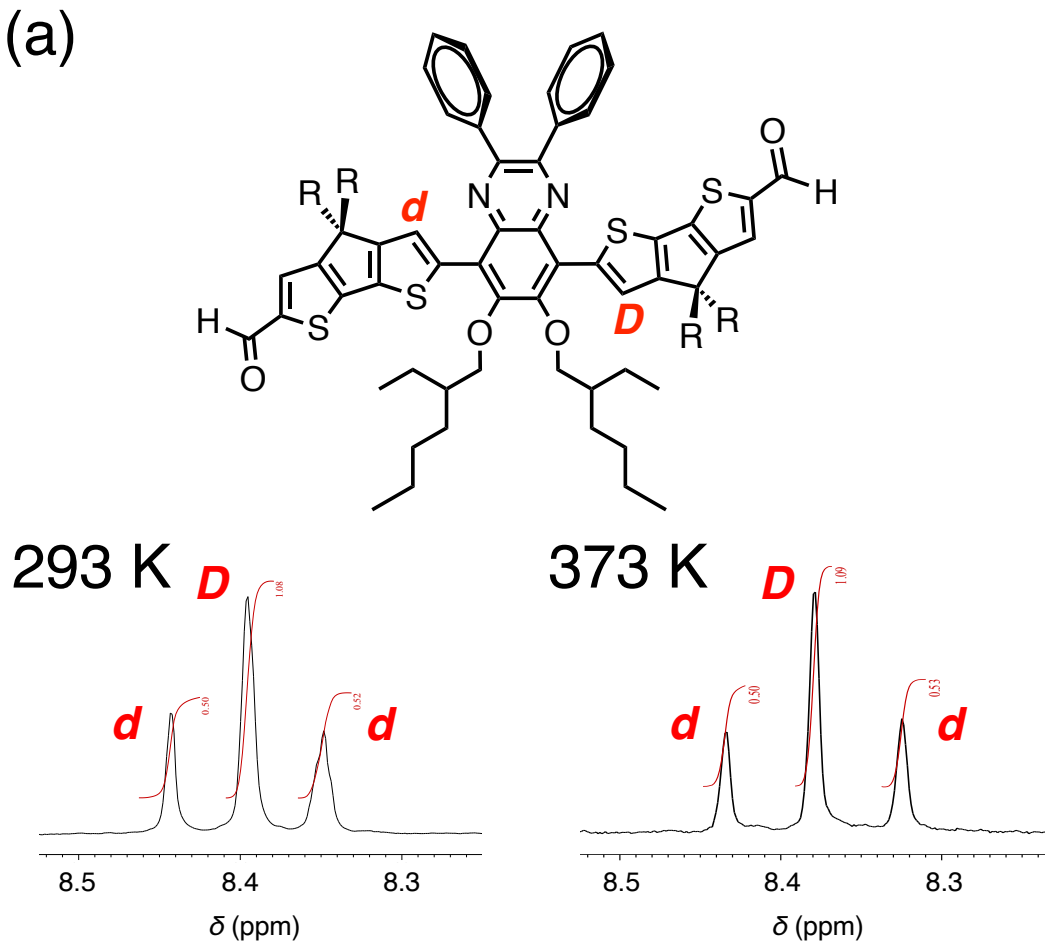
(a)
R
R
d
N
N
S
S
O
H
H
O
S
S
O
O
D
R
R
293 K
D
d
d
0.50
1.08
0.52
8.5
8.4
8.3
δ (ppm)
373 K
D
d
d
0.50
1.09
0.53
8.5
8.4
8.3
δ (ppm)

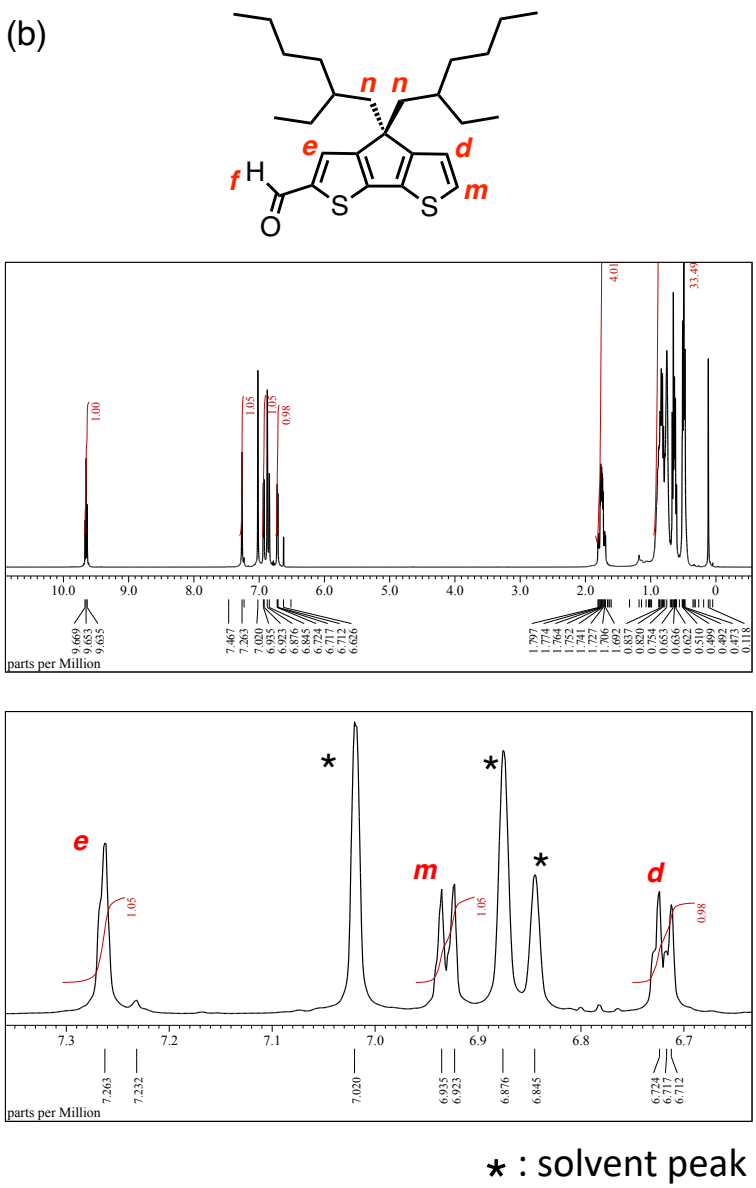

Fig. S6 (a) ^{1}H NMR spectra of CR-CPDT-CHO in C_6D_5Cl at 293 K and 373 K, focusing on the β-proton of the thiophene ring adjacent to the Qx core. In contrast to the spectrum in $CDCl_3$ (Figs. 3a and S4), each of the three signals appears as a singlet. (b) ^{1}H NMR spectrum of CPDT-CHO in C_6D_5Cl at 293 K with some peak assignments. In contrast to the spectrum in $CDCl_3$ (Fig. S3a), the signal of the thiophene β-proton (***e***) adjacent to the formyl group appeared as a singlet, while the signal of the other thiophene β-proton (***d***) appeared as a slightly distorted doublet. Similar to CR-CPDT-CHO in C_6D_5Cl, no splitting of the thiophene β-protons, due to the chirality of the two 2-ethylhexyl groups, was observed. Although the detailed reason for this solvent-dependent behavior in the ^{1}H NMR signals for thiophene β-protons of CPDT derivatives remains unclear at this stage, the presence or absence of an aromatic ring in the solvent molecule may influence the interaction between the 2-ethylhexyl group and the thiophene units of CPDT.

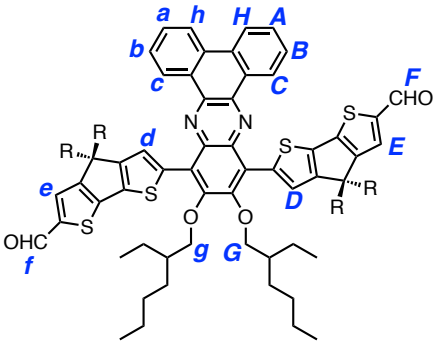
a h H A
b
B
c
C
F
CHO
N
N
R
R
d
S
S
E
e
S
D
R
R
O
O
OHC
f
g G

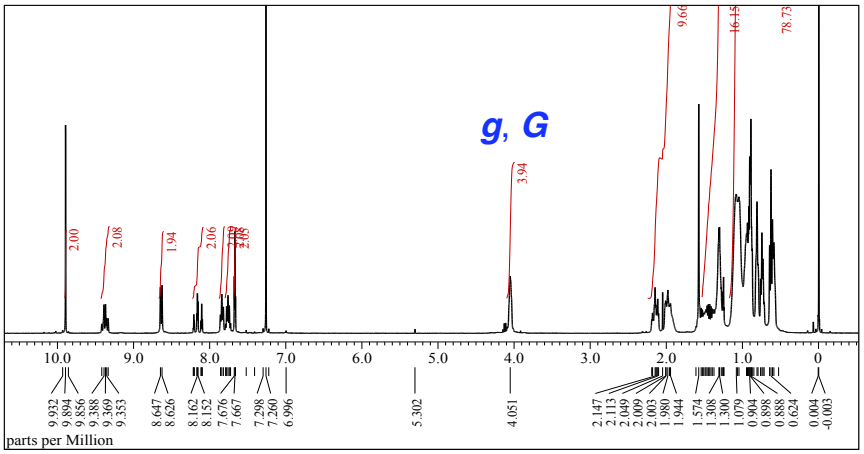
g, G
3.94
2.00
2.08
1.94
2.06
9.66
16.15
78.73
10.0
9.0
8.0
7.0
6.0
5.0
4.0
3.0
2.0
1.0
0
parts per Million

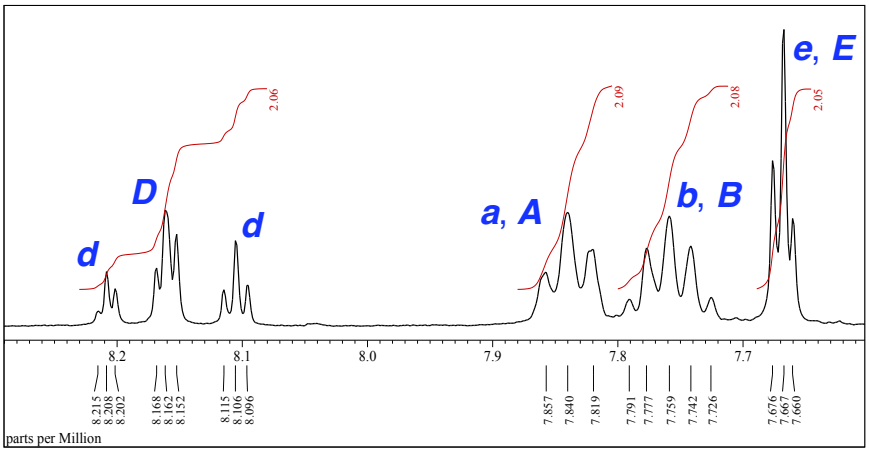
e, E
D
d
d
a, A
b, B
2.06
2.09
2.08
2.05
8.2
8.1
8.0
7.9
7.8
7.7
parts per Million

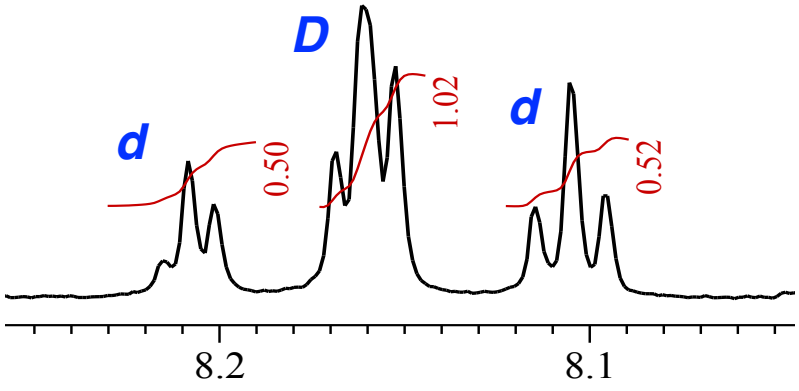
D
d
d
1.02
0.50
0.52
8.2
8.1

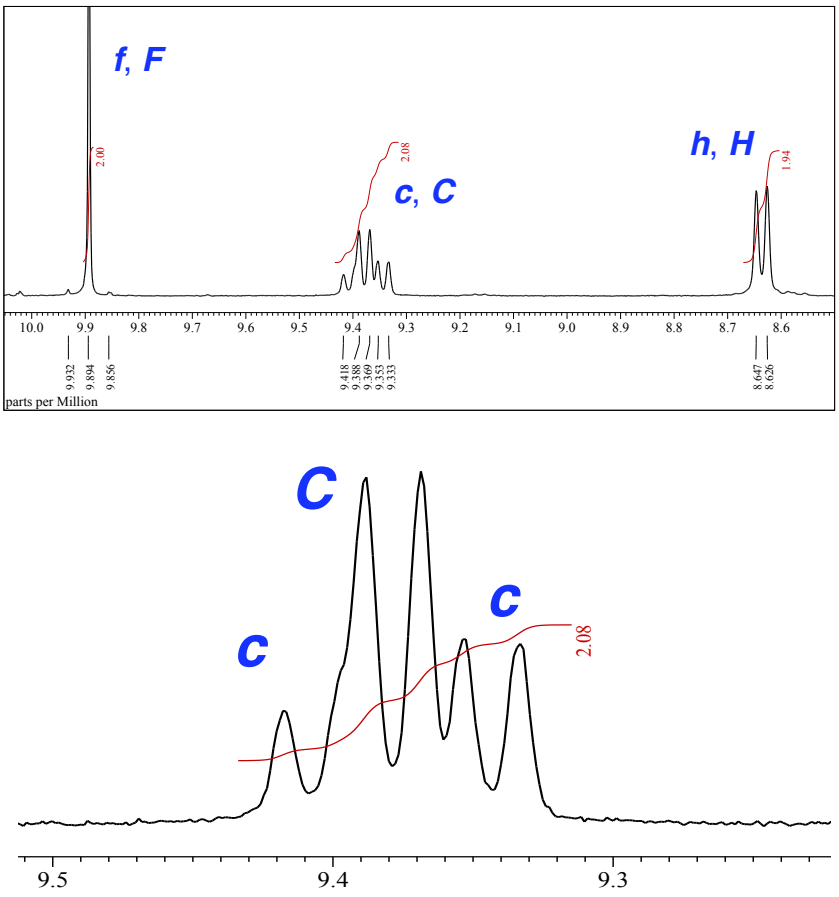

Fig. S7 ^{1}H NMR spectra of BR-CPDT-CHO in $CDCl_3$ with some peak assignments.

(a)

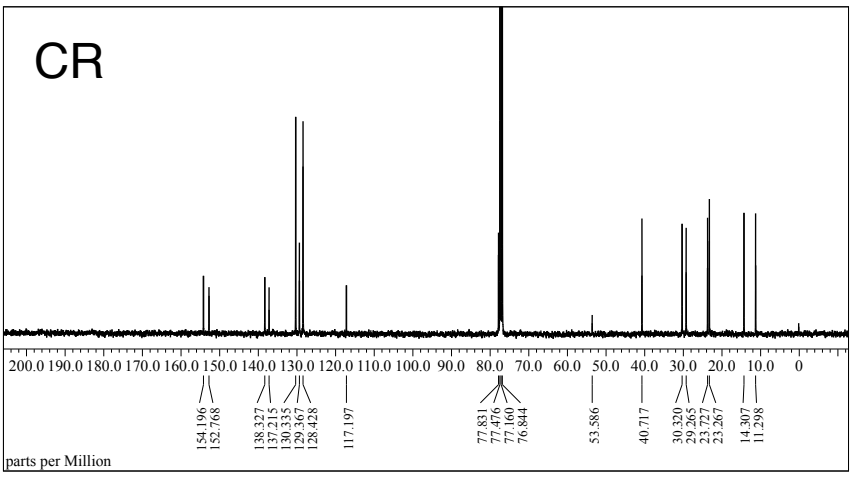
CR
200.0 190.0 180.0 170.0 160.0 150.0 140.0 130.0 120.0 110.0 100.0 90.0 80.0 70.0 60.0 50.0 40.0 30.0 20.0 10.0 0
154.196
152.768
138.327
137.215
130.335
129.367
128.428
117.197
77.831
77.476
77.160
76.844
53.586
40.717
30.320
29.265
23.727
23.267
14.307
11.298
parts per Million

(b)

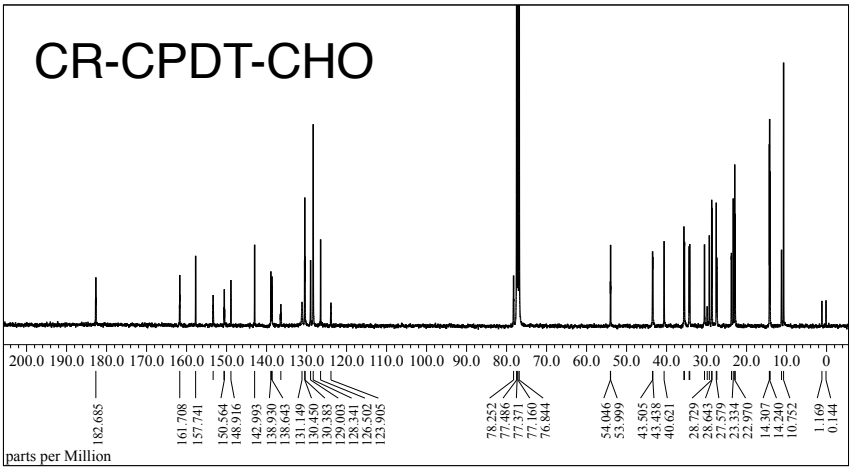
CR-CPDT-CHO
200.0 190.0 180.0 170.0 160.0 150.0 140.0 130.0 120.0 110.0 100.0 90.0 80.0 70.0 60.0 50.0 40.0 30.0 20.0 10.0 0
182.685
161.708
157.741
150.564
148.916
142.993
138.930
138.643
131.149
130.450
130.383
129.903
129.041
126.502
123.905
78.252
77.486
77.371
77.160
76.844
54.046
53.999
43.505
43.438
40.621
28.729
28.643
27.579
23.334
22.970
14.307
14.240
10.752
1.169
0.144
parts per Million

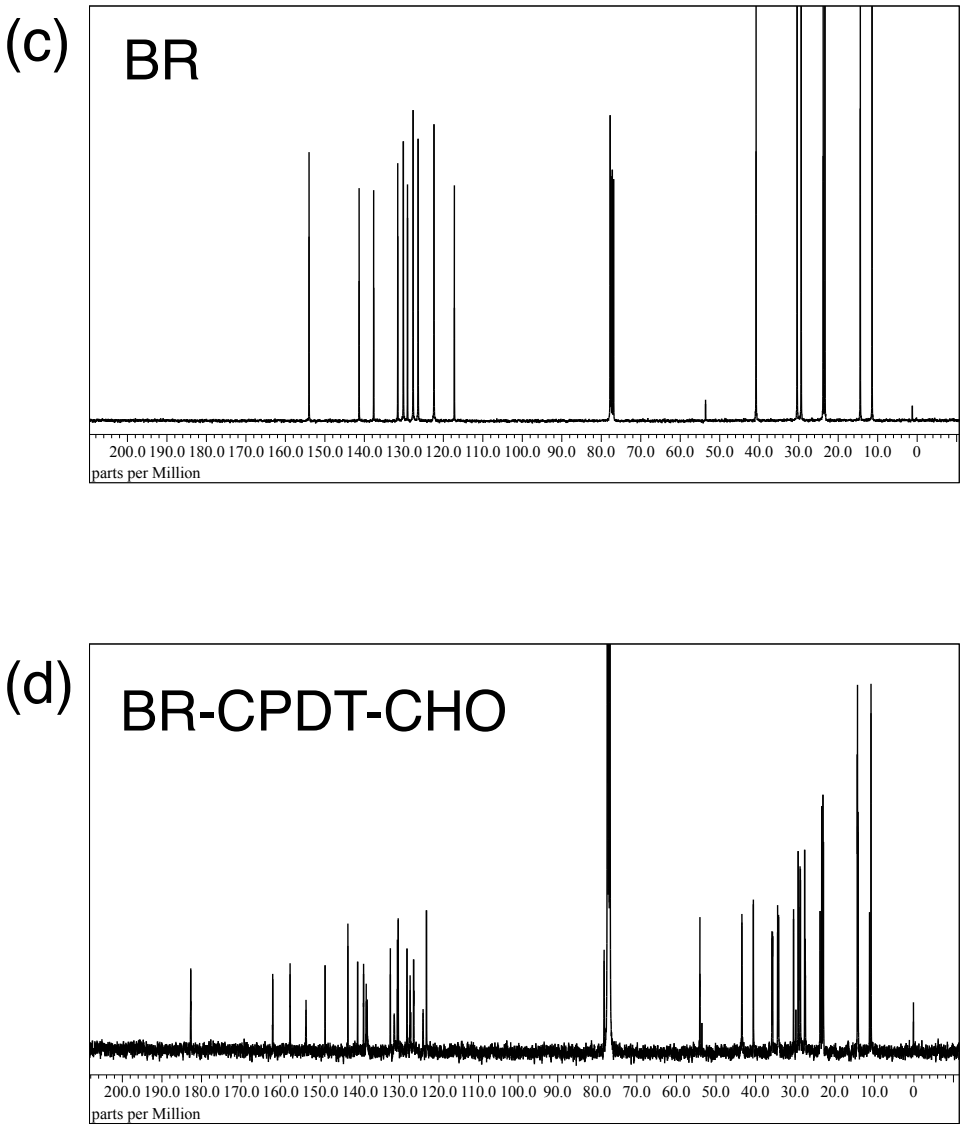

Fig. S8 ^{13}C NMR spectra of (a) CR, (b) CR-CPDT-CHO, (c) BR, and (d) BR-CPDT-CHO in $CDCl_3$.

(a)

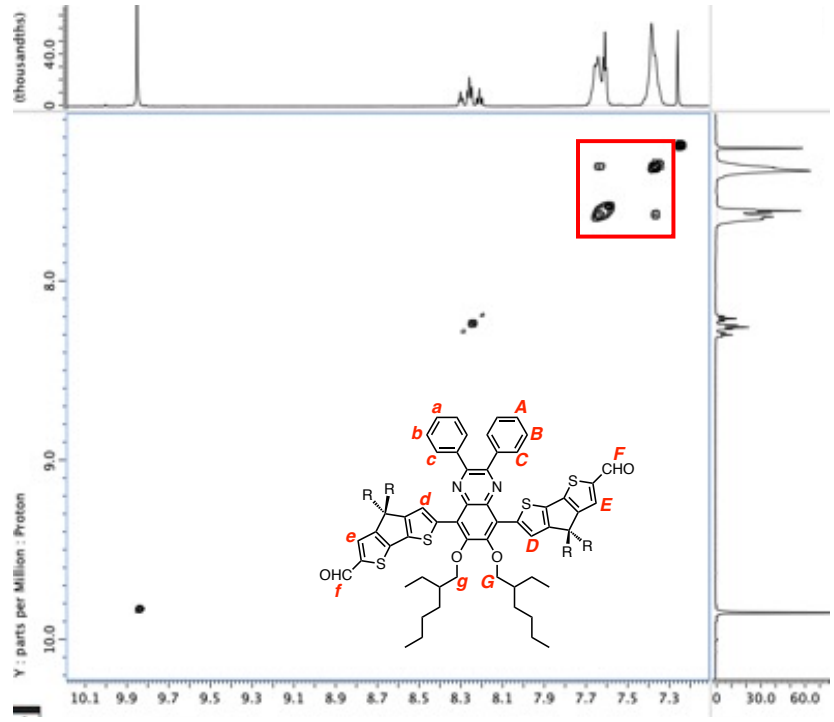
(thousandths)
40.0
0
8.0
9.0
10.0
Y : parts per Million : Proton
10.1 9.9 9.7 9.5 9.3 9.1 8.9 8.7 8.5 8.3 8.1 7.9 7.7 7.5 7.3
0 30.0 60.0
a
b
c
A
B
C
d
e
f
g
G
D
E
F
CHO
OHC
R
R
S
N
O

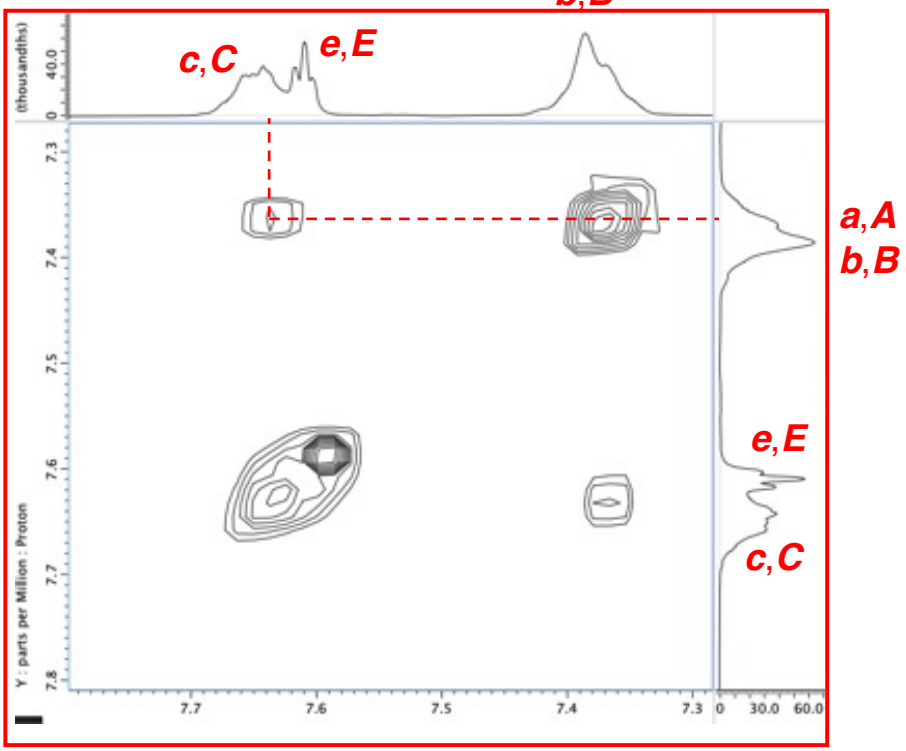
a,A
b,B
c,C
e,E
(thousandths)
40.0
0
7.3
7.4
7.5
7.6
7.7
7.8
Y : parts per Million : Proton
7.7 7.6 7.5 7.4 7.3
0 30.0 60.0
a,A
b,B
e,E
c,C

(b)

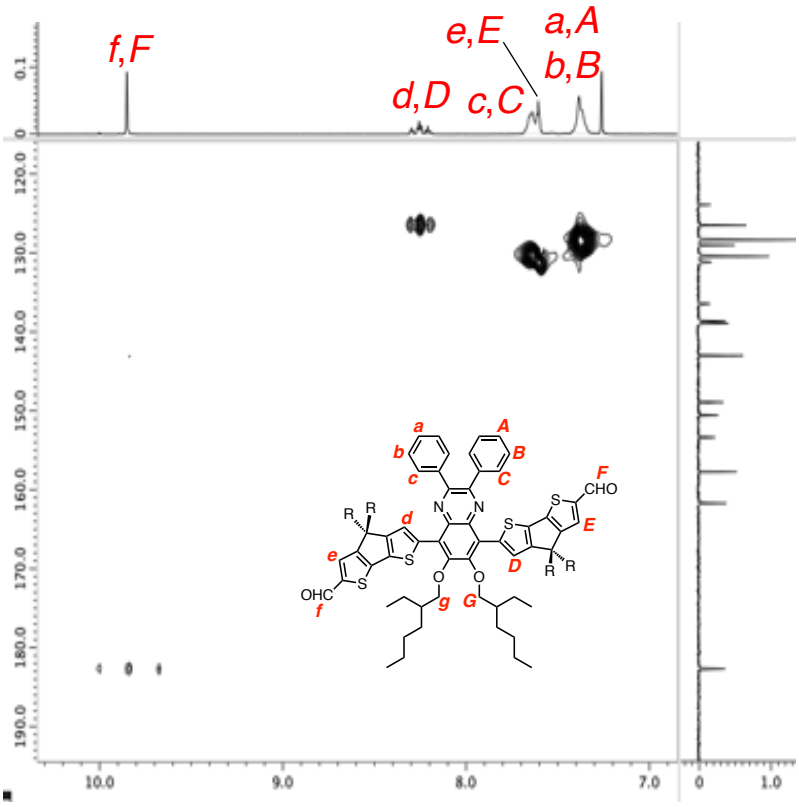
f,F
e,E
a,A
b,B
d,D
c,C
a
A
b
B
c
C
F
CHO
R
R
d
N
N
S
S
E
e
S
D
R
R
OHC
f
O
O
g
G

(c)

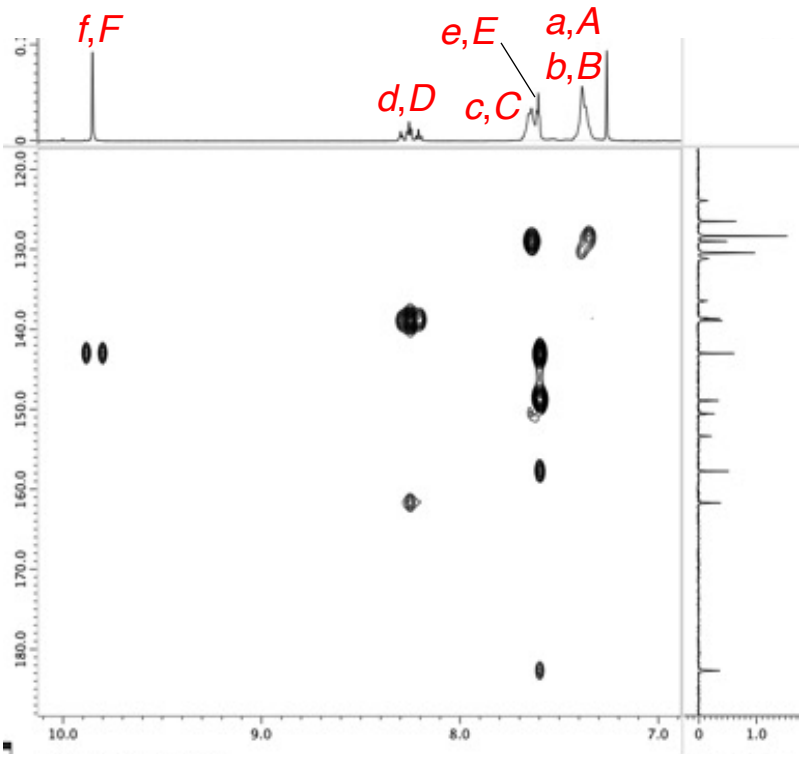
f,F
e,E
a,A
b,B
d,D
c,C

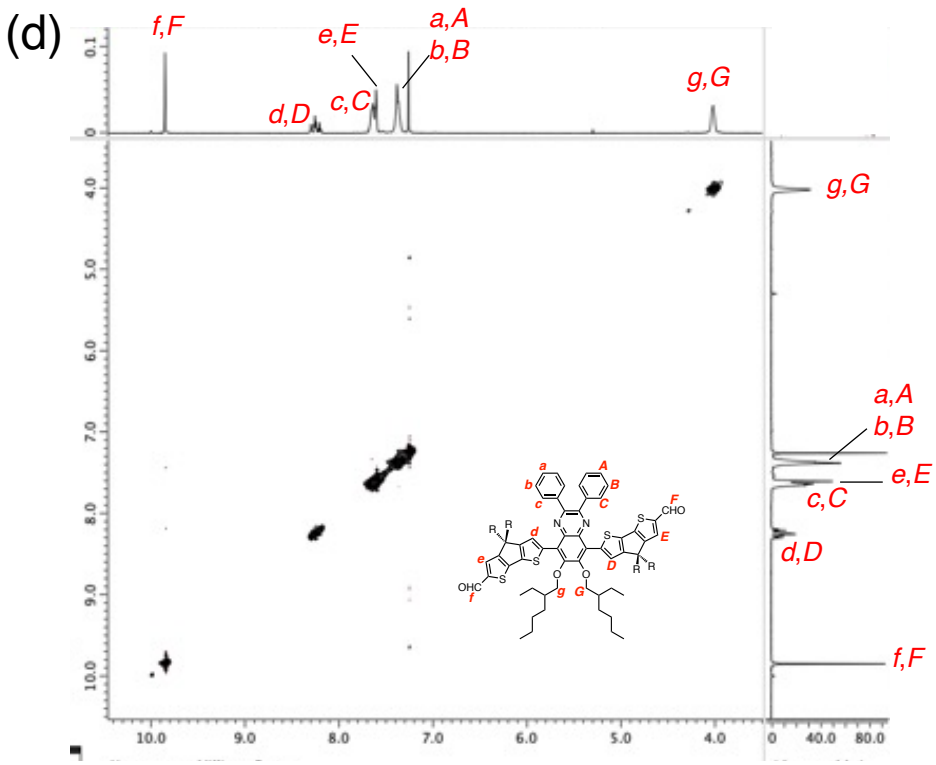

Fig. S9 (a) ^{1}H-^{1}H COSY, (b) ^{1}H-^{13}C HSQC, (c) ^{1}H-^{13}C HMBC (formyl and aromatic regions), and (d) NOESY (formyl, aromatic, and OCH_2 regions) spectra of CR-CPDT-CHO in $CDCl_3$. In (a), cross peaks between the phenyl protons (***a***/***A***, ***b***/***B***, and ***c***/***C***) are observed. In (d), no interaction is observed between ***c*** and ***d***, as well as between ***D*** and ***G***. This result suggests that due to the twisting between the Qx core and CPDT, ***c*** and ***d***, as well as ***D*** and ***G***, are spatially separated.

(a)

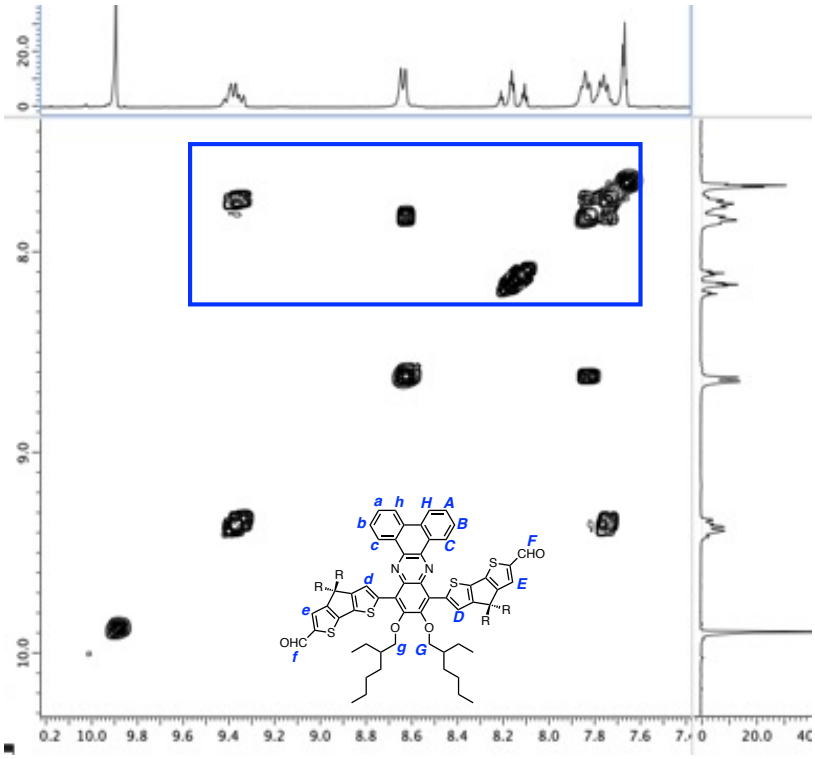
a h H A
b B
c C
F
CHO
d
R
R
e
S
S
E
D
R
R
OHC
f
O
O
g G
N
N
S
S

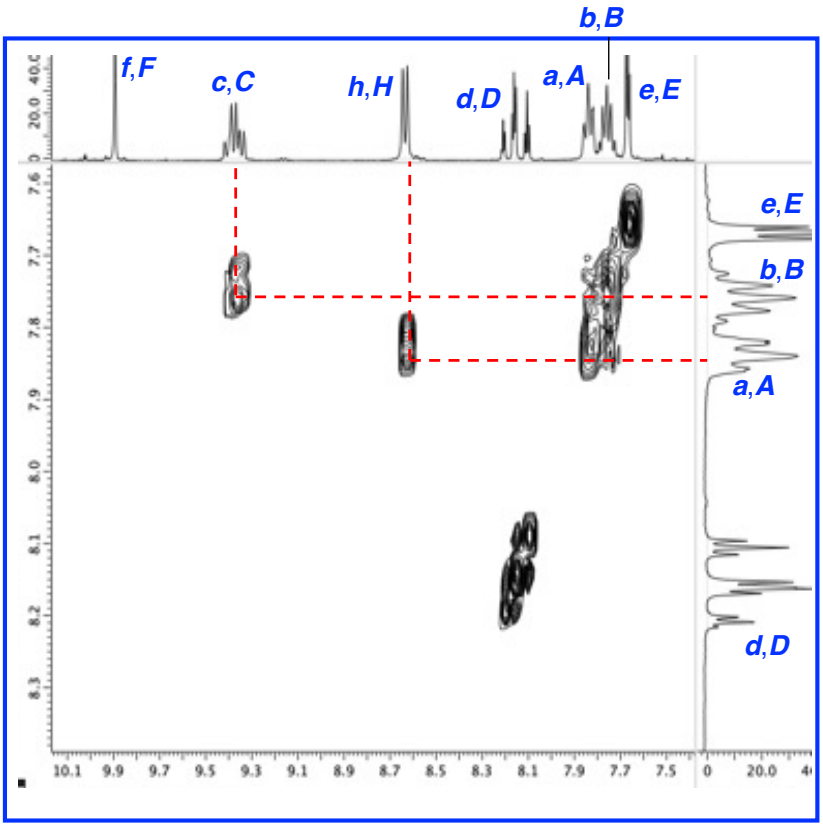
b,B
f,F
c,C
h,H
d,D
a,A
e,E
e,E
b,B
a,A
d,D

(b)

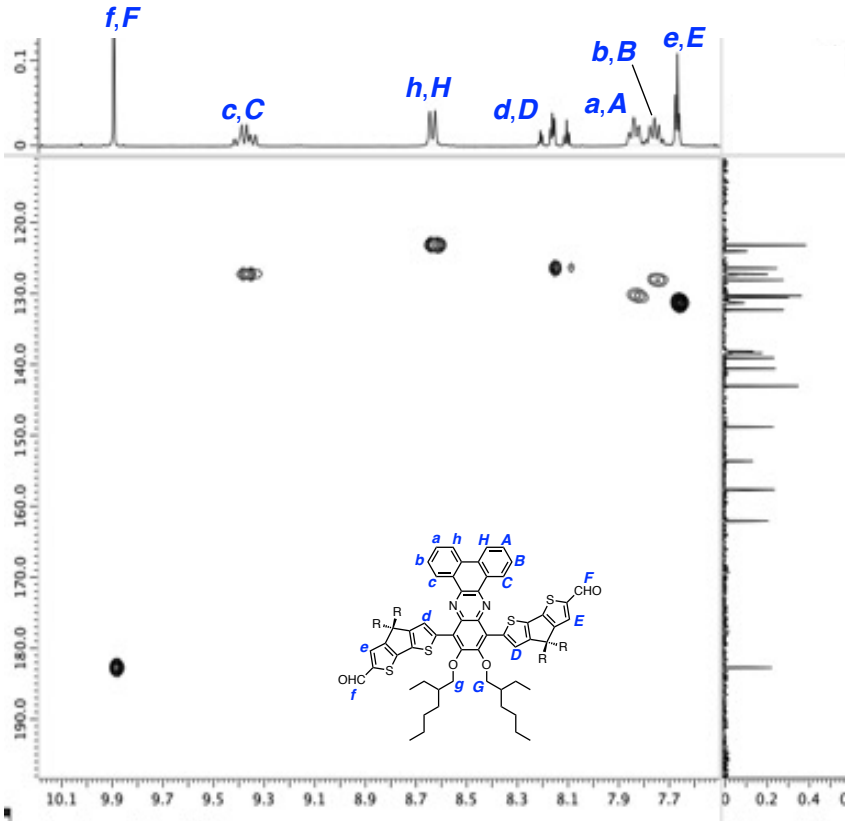
f,F
c,C
h,H
d,D
a,A
b,B
e,E
a h H A
b B
c C
d
e
f
g G
D
E
F
CHO
OHC
R
S
N
O

(c)

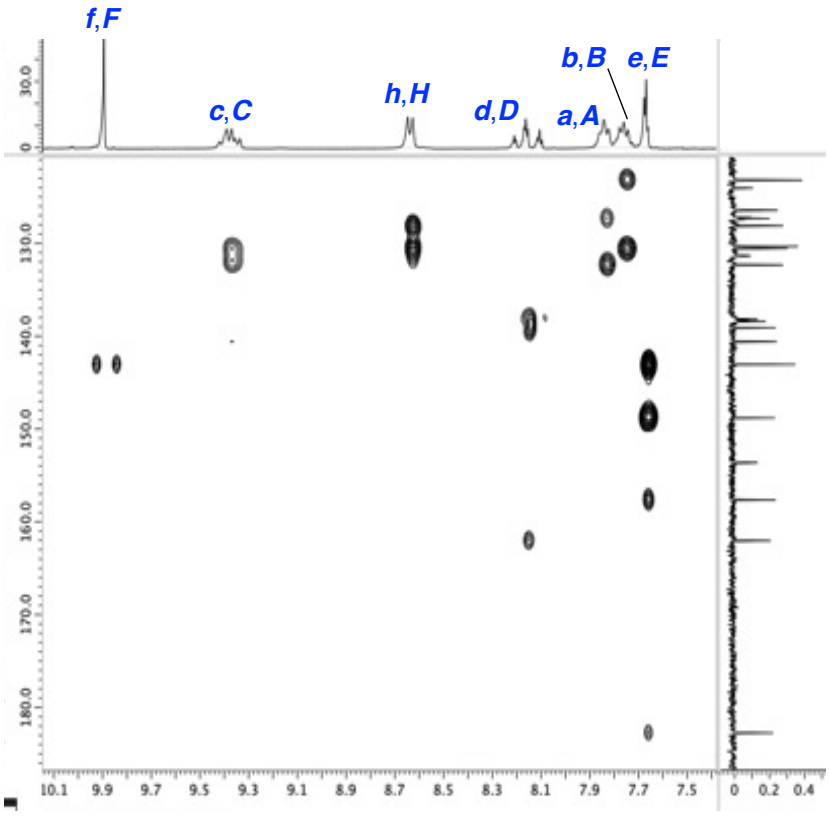
f,F
c,C
h,H
d,D
a,A
b,B
e,E

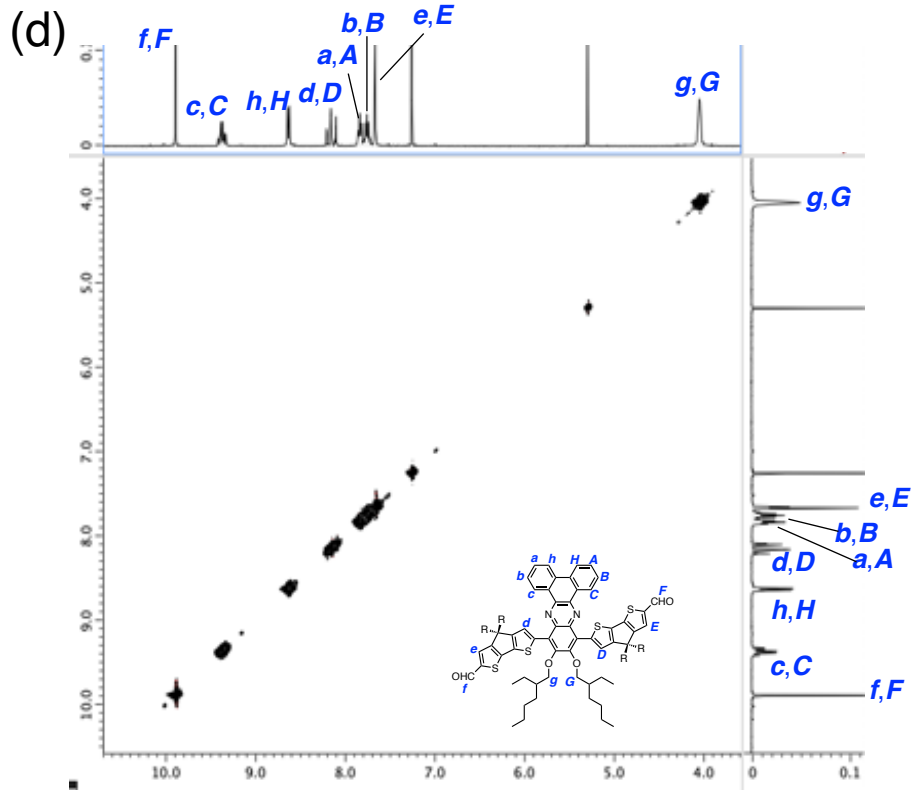

Fig. S10 (a) ^{1}H-^{1}H COSY, (b) ^{1}H-^{13}C HSQC, (c) ^{1}H-^{13}C HMBC (formyl and aromatic regions), and (d) NOESY (formyl, aromatic, and OCH_2 regions) spectra of BR-CPDT-CHO in $CDCl_3$. In (a), cross peaks between the aromatic protons of fused phenanthrene, especially between ***c***/***C*** and ***b***/***B***, as well as between ***h***/***H*** and ***a***/***A*** are observed. In (d), no interaction is observed between ***c*** and ***d***, as well as between ***D*** and ***G***. This result suggests that due to the twisting between the Qx core and CPDT, ***c*** and ***d***, as well as ***D*** and ***G***, are spatially separated.

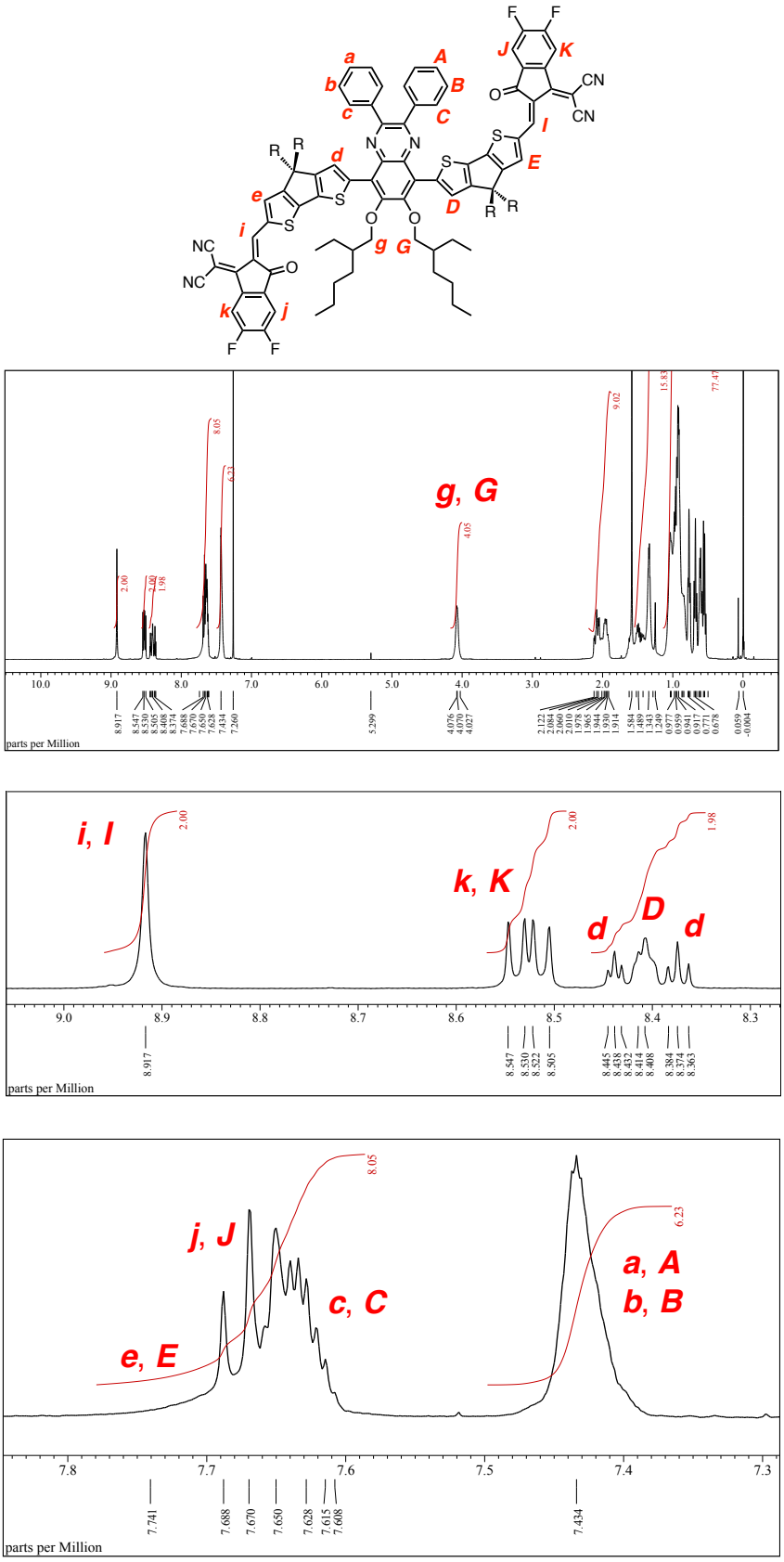

Fig. S11 ^{1}H NMR spectra of CRIC in $CDCl_3$ with some peak assignments.

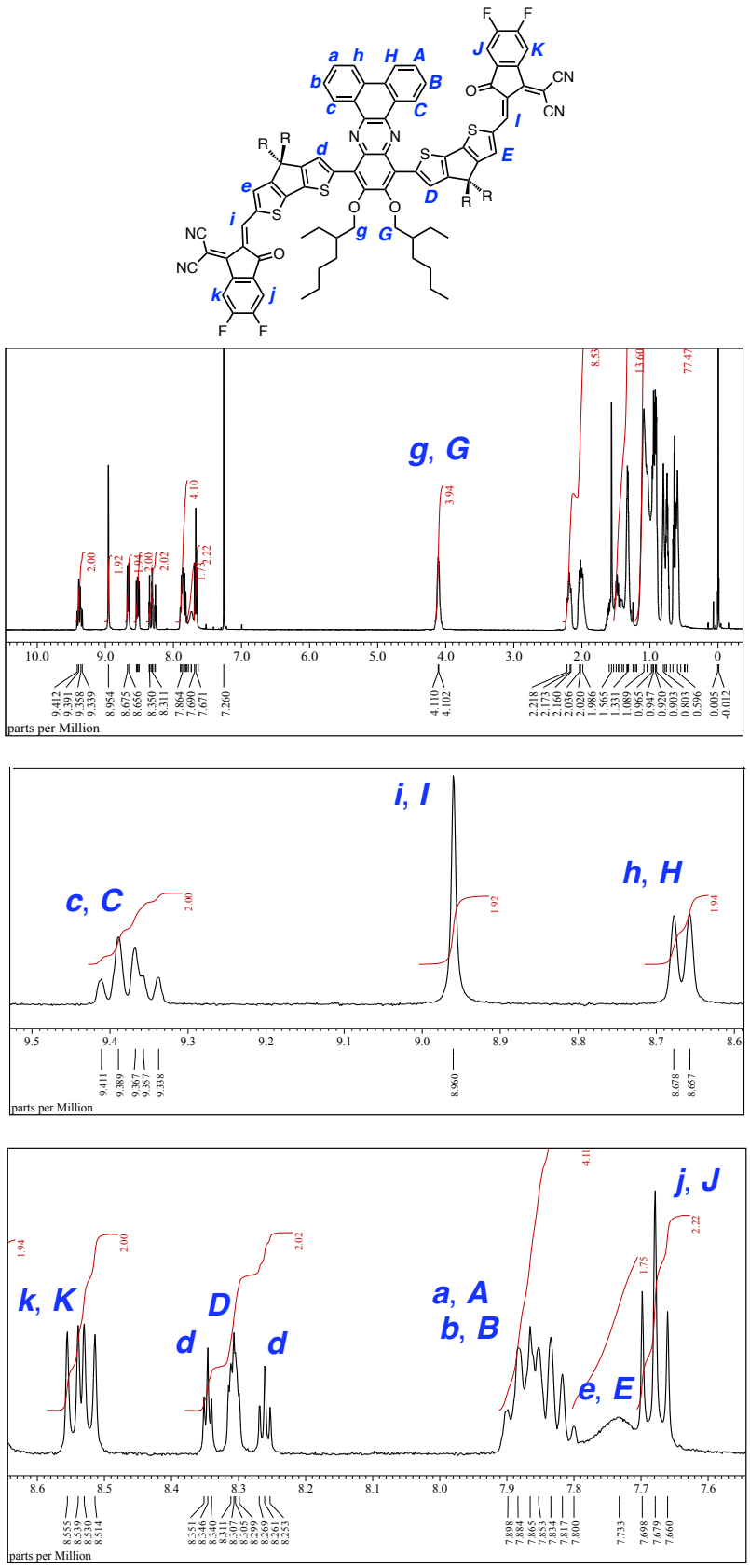

Fig. S12 ^{1}H NMR spectra of BRIC in $CDCl_3$ with some peak assignments.

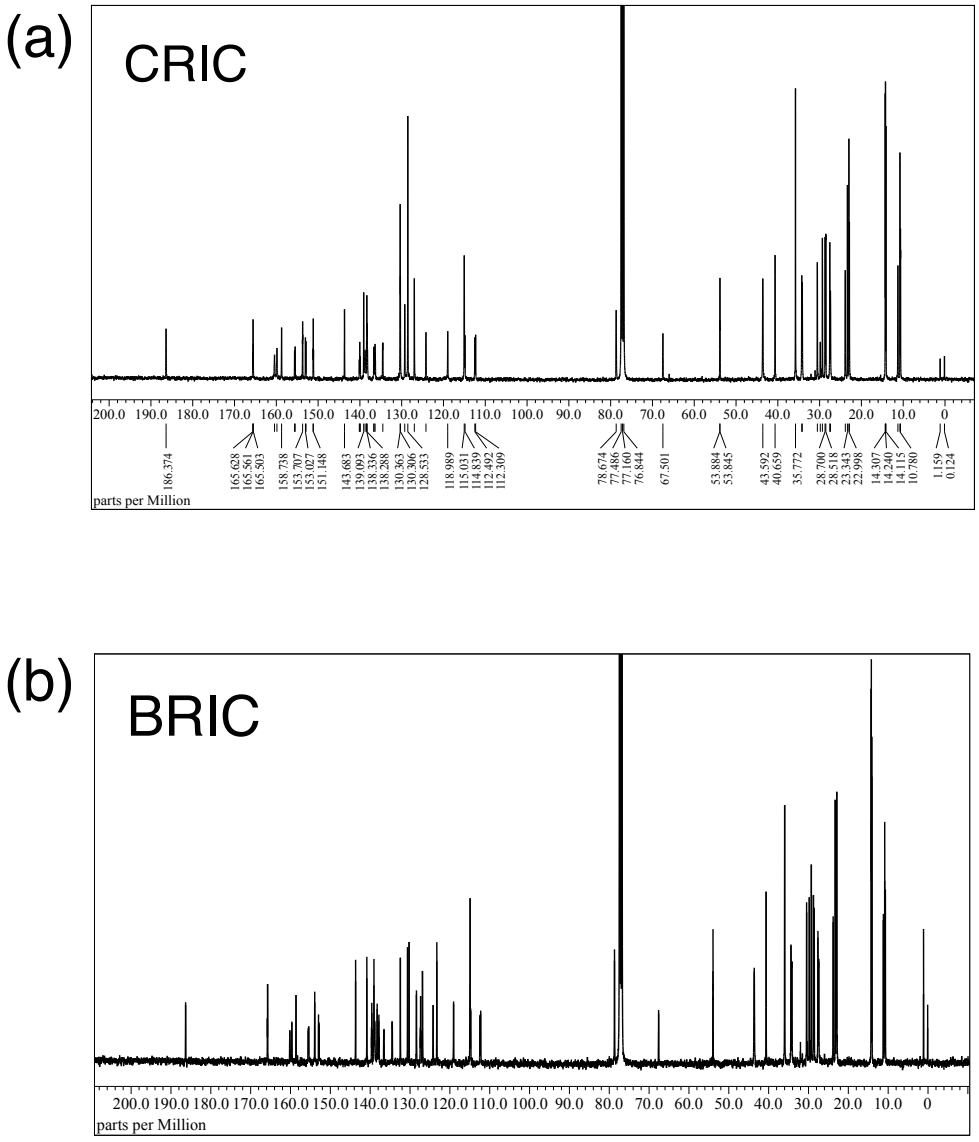

Fig. S13 ^{13}C NMR spectra of (a) CRIC and (b) BRIC in $CDCl_3$.

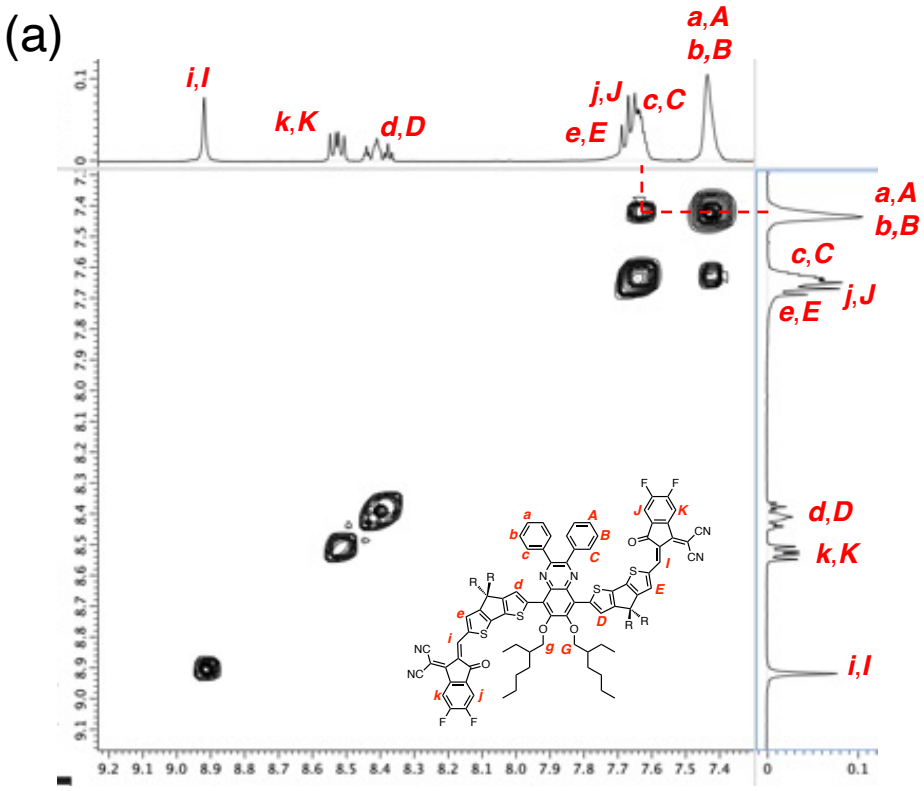
(a)
a,A
b,B
i,I
k,K
d,D
j,J
c,C
e,E
a,A
b,B
c,C
j,J
e,E
d,D
k,K
i,I
(b)
a,A
b,B
i,I
k,K
d,D
j,J
c,C
e,E

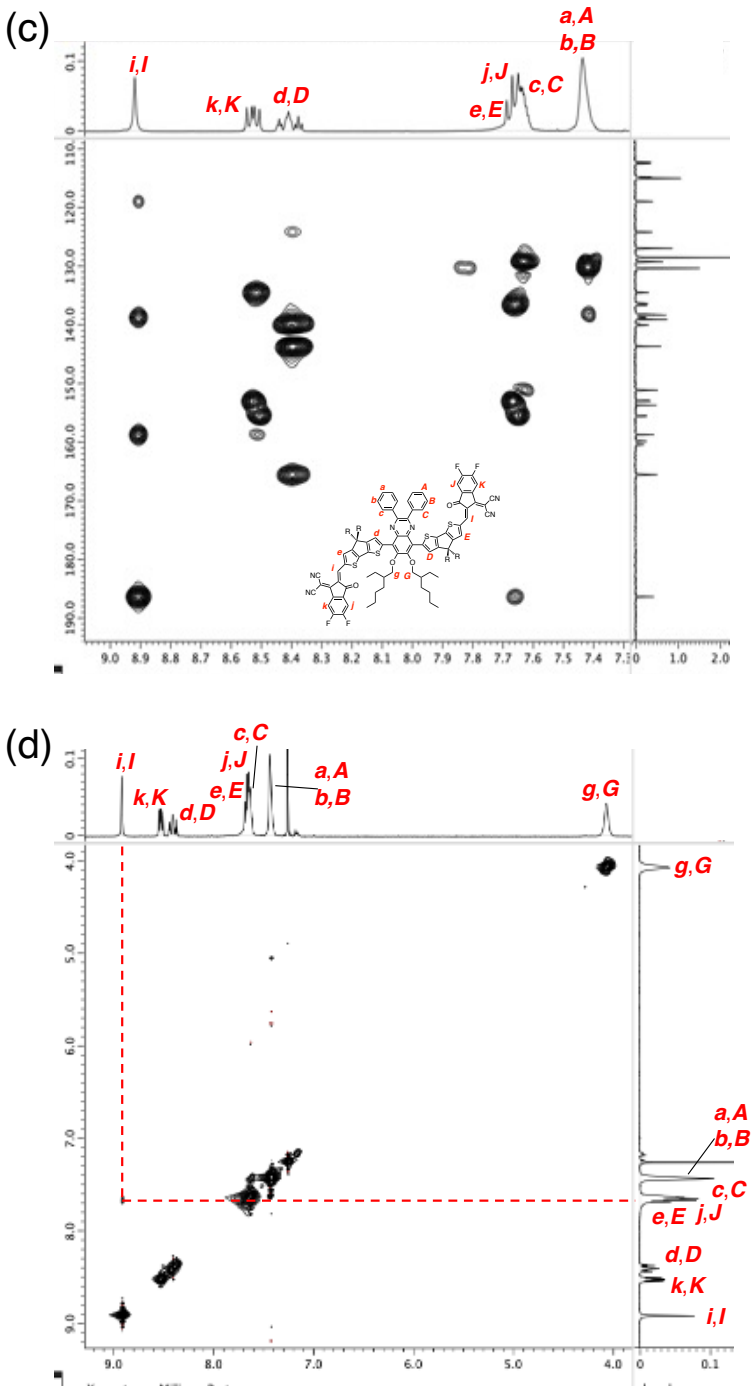

Fig. S14 (a) ^{1}H-^{1}H COSY, (b) ^{1}H-^{13}C HSQC, (c) ^{1}H-^{13}C HMBC (aromatic and vinyl regions), and (d) NOESY (aromatic, vinyl, and OCH_2 regions) spectra of CRIC in $CDCl_3$. In (a), cross peaks between the phenyl protons (***a***/***A***, ***b***/***B***, and ***c***/***C***) are observed. In (d), no interaction is observed between ***c*** and ***d***, as well as between ***D*** and ***G***. This result suggests that due to the twisting between the Qx core and CPDT, ***c*** and ***d***, as well as ***D*** and ***G***, are spatially separated. In addition, a cross peak between ***i***/***I*** and ***e***/***E*** was observed, reflecting their spatial proximity, which supports these peak assignments.

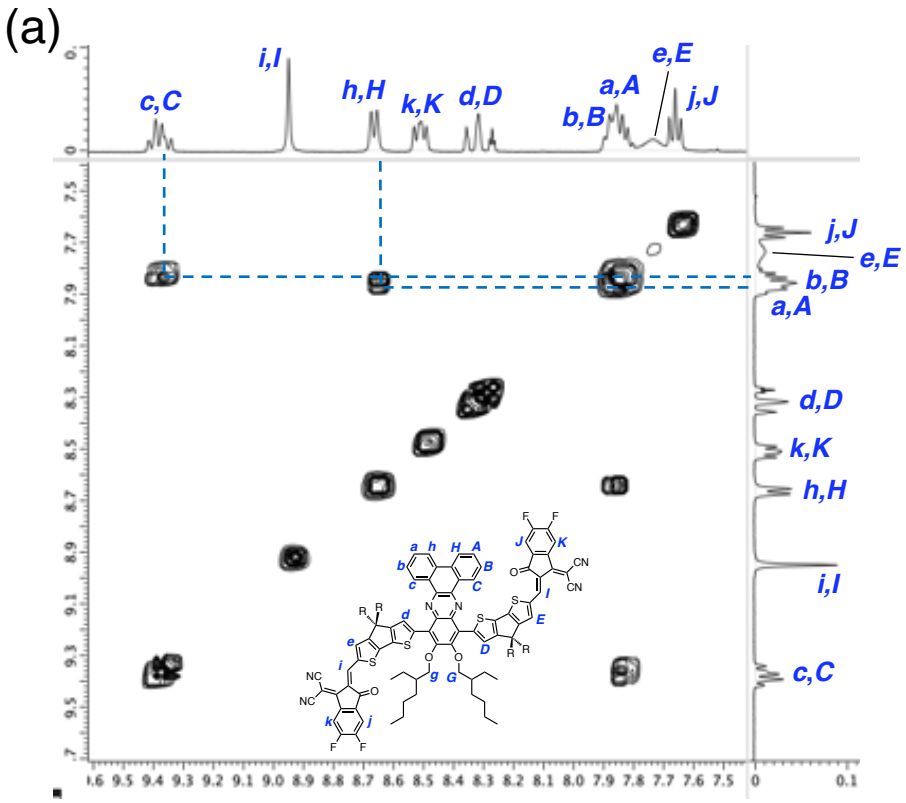
(a)
c,C
i,I
h,H
k,K
d,D
b,B
a,A
e,E
j,J
j,J
e,E
b,B
a,A
d,D
k,K
h,H
i,I
c,C

(b)

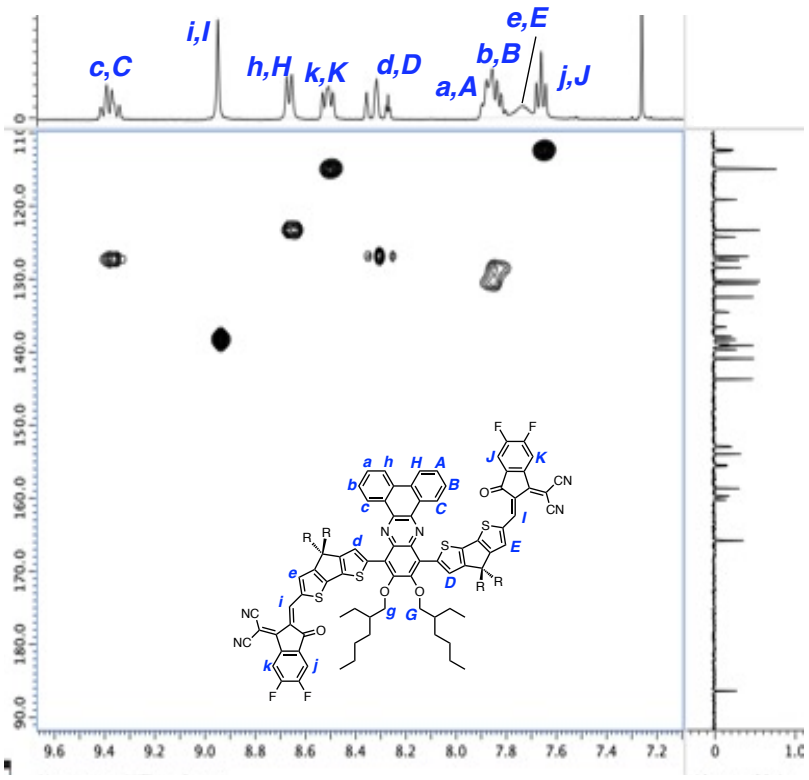
c,C
i,I
h,H
k,K
d,D
a,A
b,B
e,E
j,J
a h H A
b B
c C
d D
e E
i I
g G
J K
k j
F F
CN
CN
NC
NC
O
S
N
R R

(c)

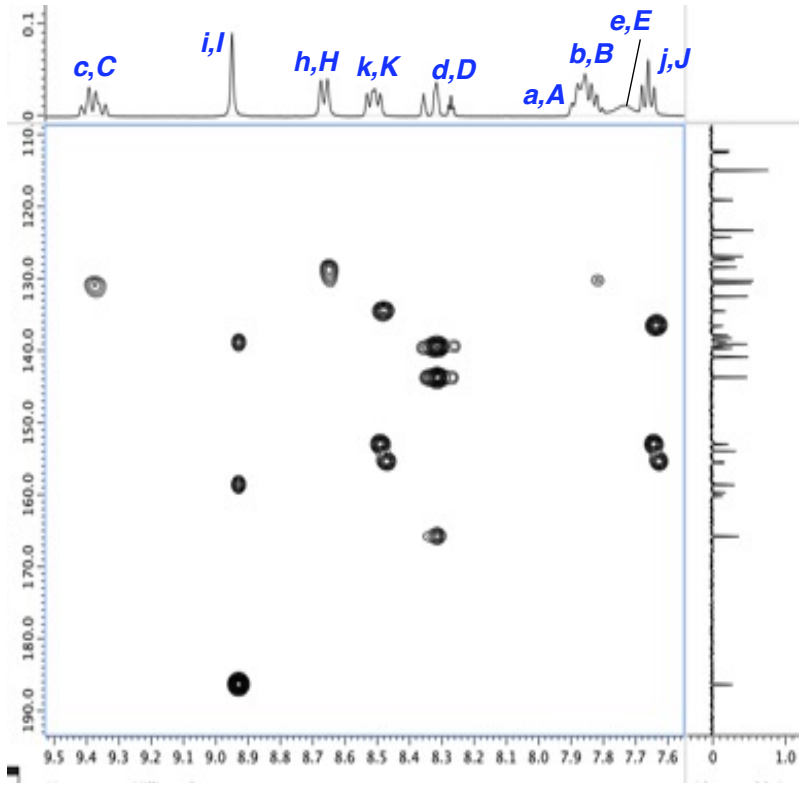
c,C
i,I
h,H
k,K
d,D
a,A
b,B
e,E
j,J

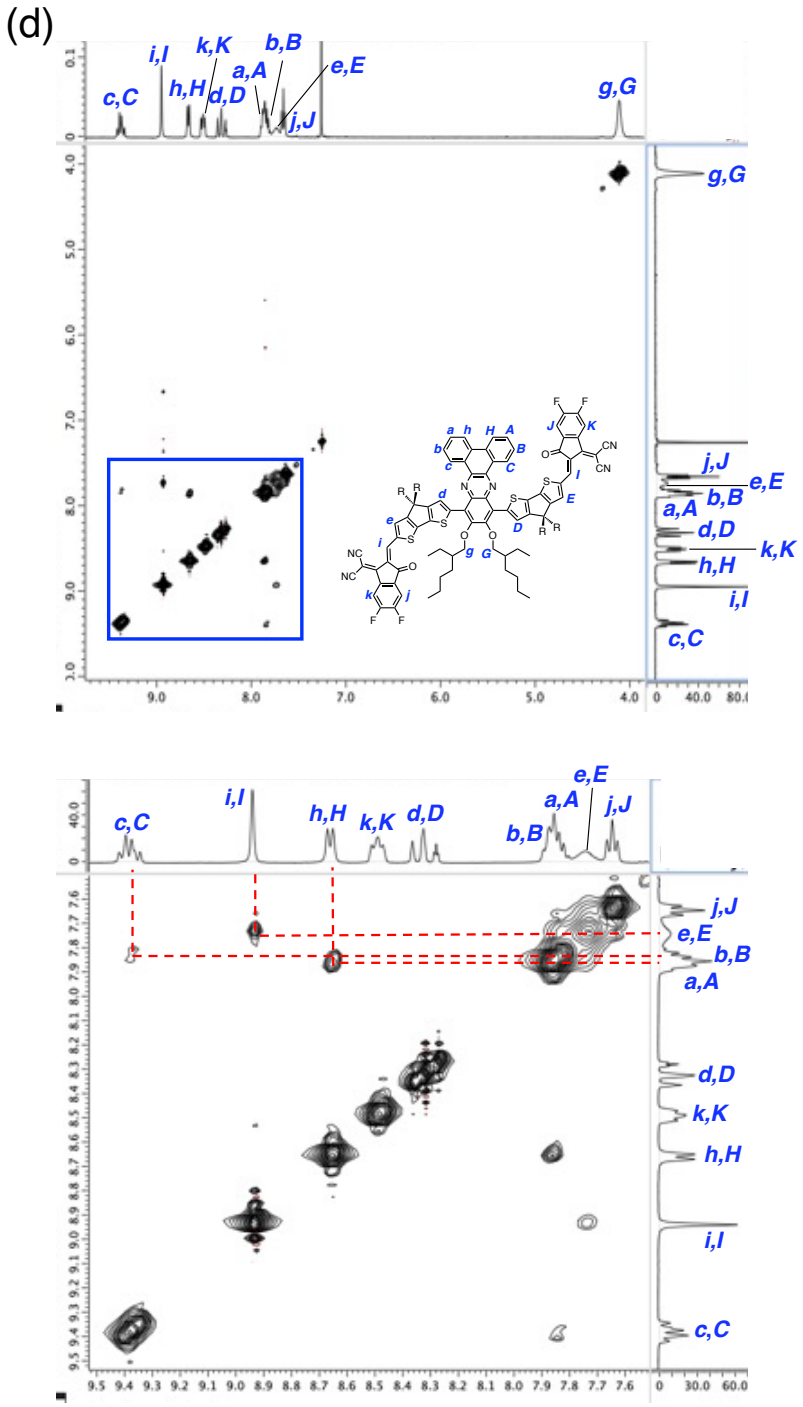

Fig. S15 (a) ^{1}H-^{1}H COSY, (b) ^{1}H-^{13}C HSQC, (c) ^{1}H-^{13}C HMBC (aromatic and vinyl regions), and (d) NOESY (aromatic, vinyl, and OCH_2 regions) spectra of BR-CPDT-CHO in $CDCl_3$. In (a), cross peaks between the aromatic protons of fused phenanthrene, especially between ***c***/***C*** and ***b***/***B***, as well as between ***h***/***H*** and ***a***/***A*** are observed. In (d), no interaction is observed between ***c*** and ***d***, as well as between ***D*** and ***G***. This result suggests that due to the twisting between the Qx core and CPDT, ***c*** and ***d***, as well as ***D*** and ***G***, are spatially separated. In addition, cross peaks between ***i***/***I*** and ***e***/***E***, as well as between the phenanthrene peaks (***c***/***C*** and ***b***/***B***, ***h***/***H*** and ***a***/***A***) were observed.

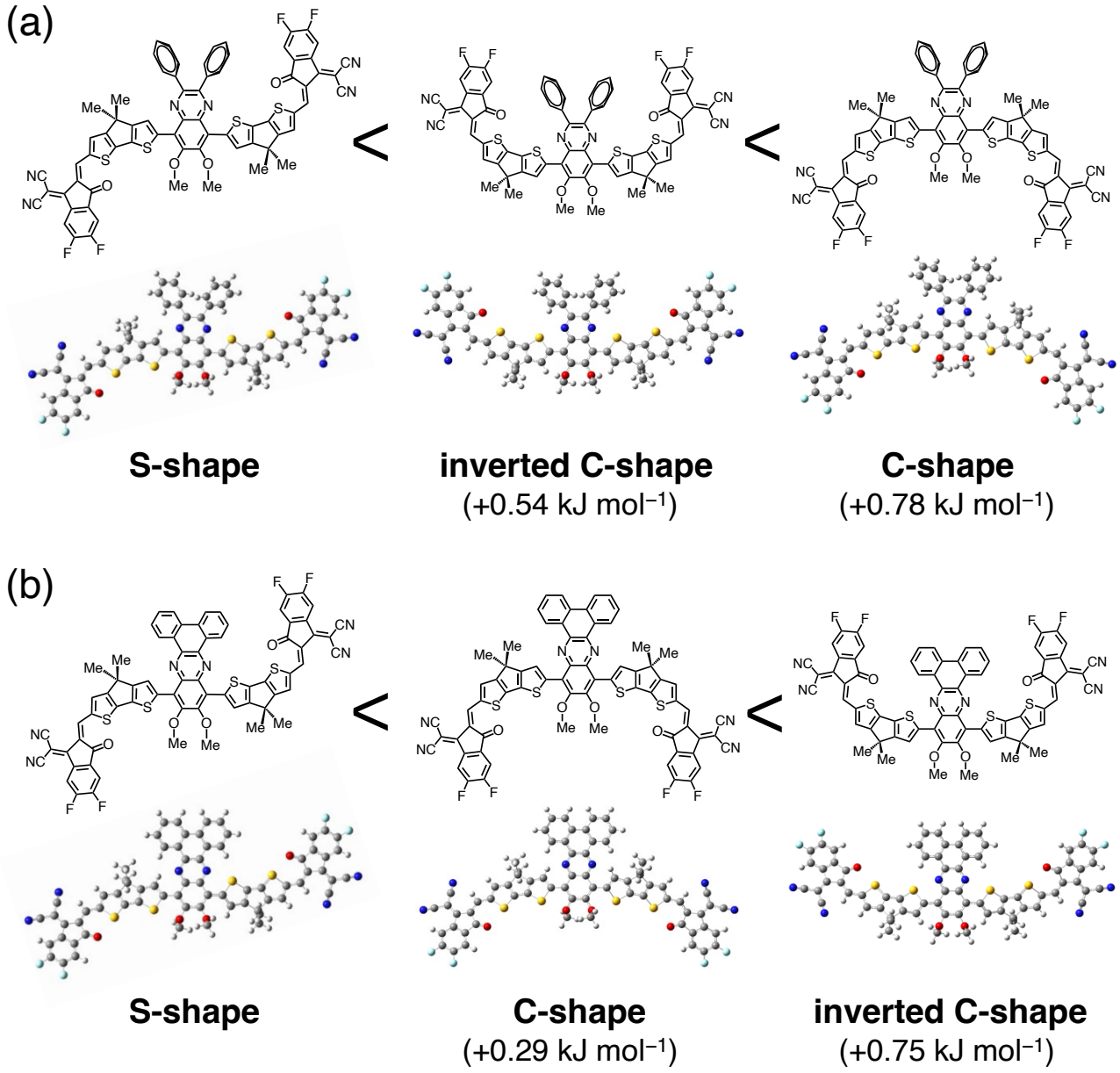

Fig. S16 Chemical structures and optimized geometries of S-, inverted C-, and C-shaped conformations for (a) CRIC and (b) BRIC models with methyl groups. The energies were calculated based on DFT at the B3LYP/6-31G(d) level. The values in parentheses are energies relative to the S-shaped conformation.

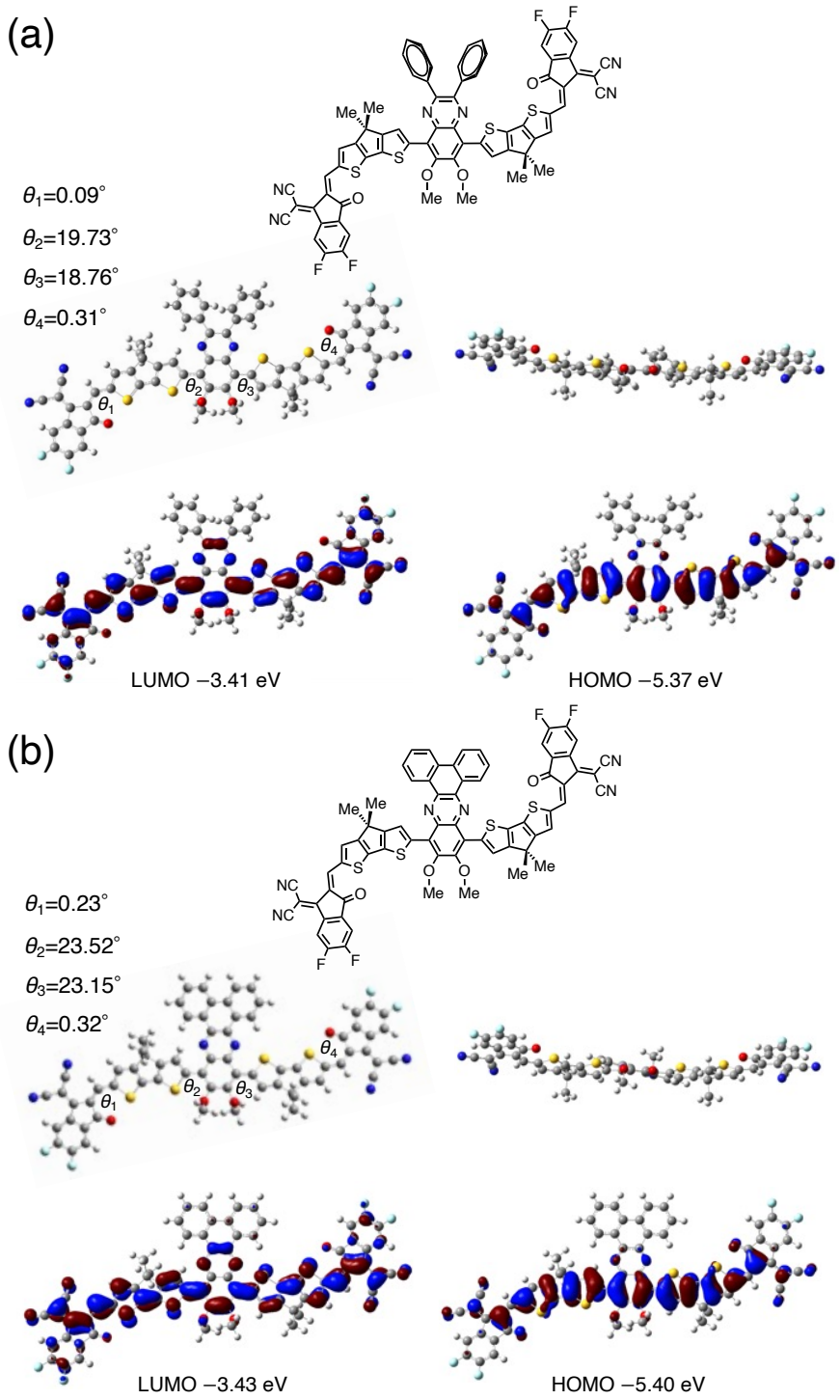

Fig. S17 Chemical structures, optimized geometries (top and side views), and contour plots of frontier molecular orbitals simulated by the DFT calculations using the B3LYP/6-31G(d) model for the simplified (a) CRIC and (b) BRIC. Alkyl chains were simplified as methyl groups. Calculated energy levels are shown below the corresponding depictions.

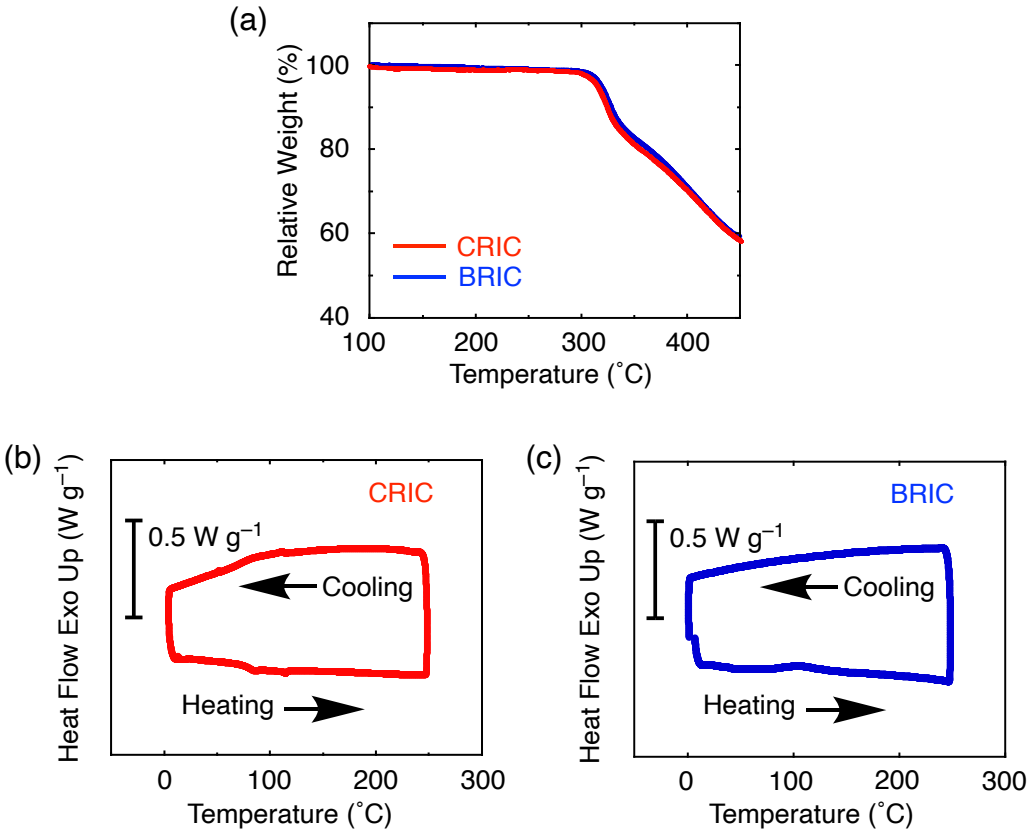

Fig. S18 (a) TGA curves of CRIC and BRIC. DSC curves of (b) CRIC and (c) BRIC. The analyses were performed under flowing nitrogen at a scan rate of 10 °C min^{-1}. The decomposition temperatures (5% weight loss) of CRIC and BRIC were 315 and 318°C, respectively.

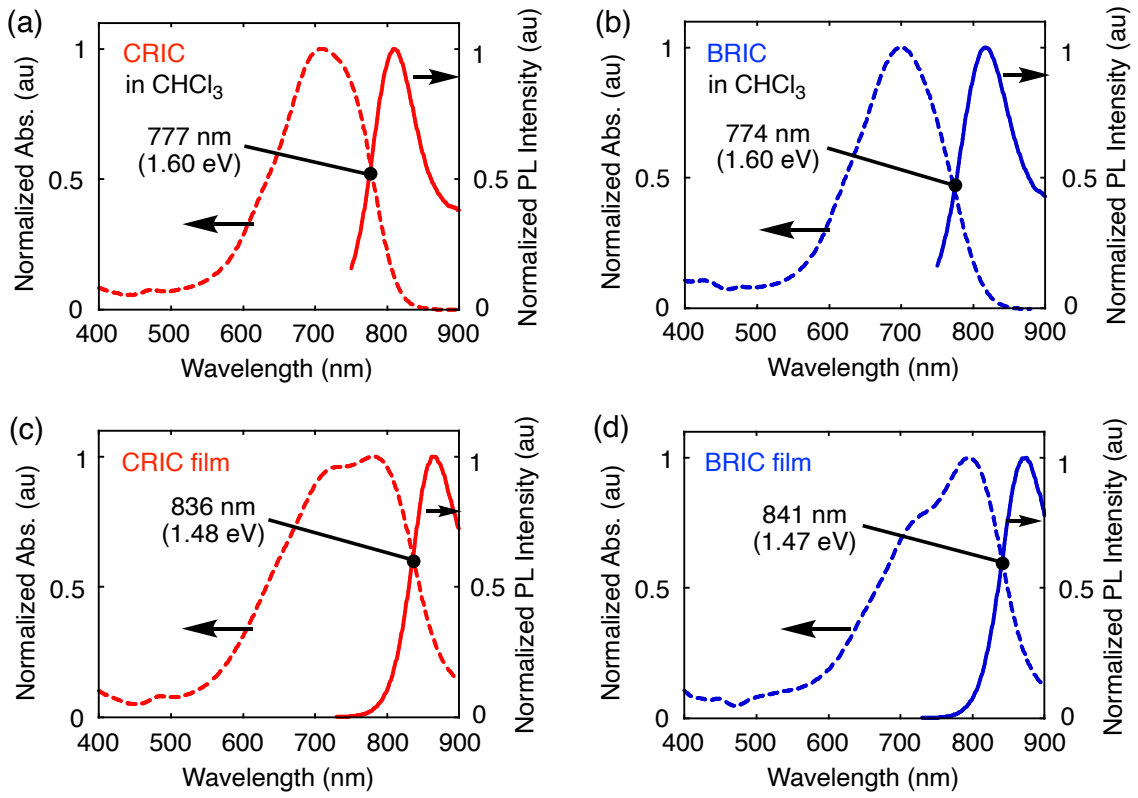

Fig. S19 (a) Normalized UV–vis–NIR absorption and photoluminescence (PL) spectra of (a) CRIC in chloroform, (b) BRIC in chloroform, (c) CRIC film, and (d) BRIC film. The PL measurements were performed using excitation wavelengths corresponding to the absorption maxima. The wavelengths and energies at the intersection points are shown in the figures.

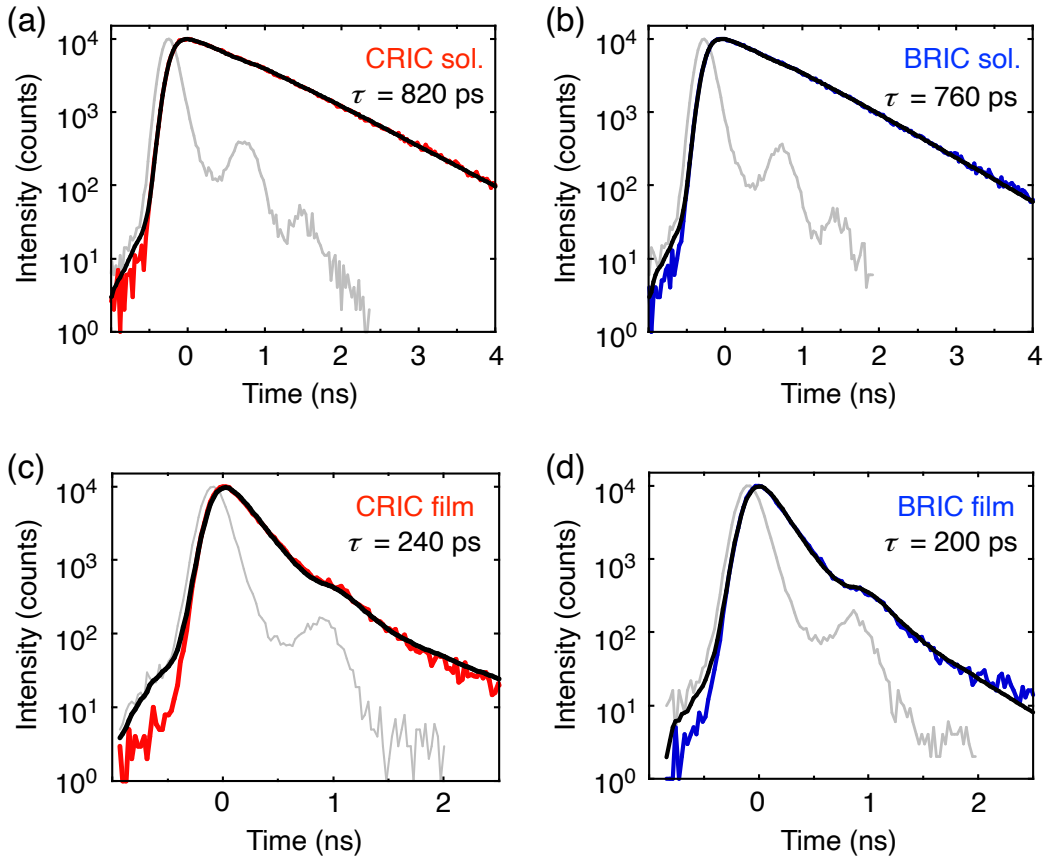

Fig. S20 Nanosecond fluorescence decay (red or blue line), decay fitting (black line), and instrumental response function (gray line) of (a) CRIC in $CHCl_3$, (b) BRIC in $CHCl_3$, (c) CRIC film, and (d) BRIC film, measured by the TCSPC technique. The excitation wavelength was 636 nm. The emission was detected at the maximum wavelength. The fluorescence lifetimes (τ) are also shown in the figures.

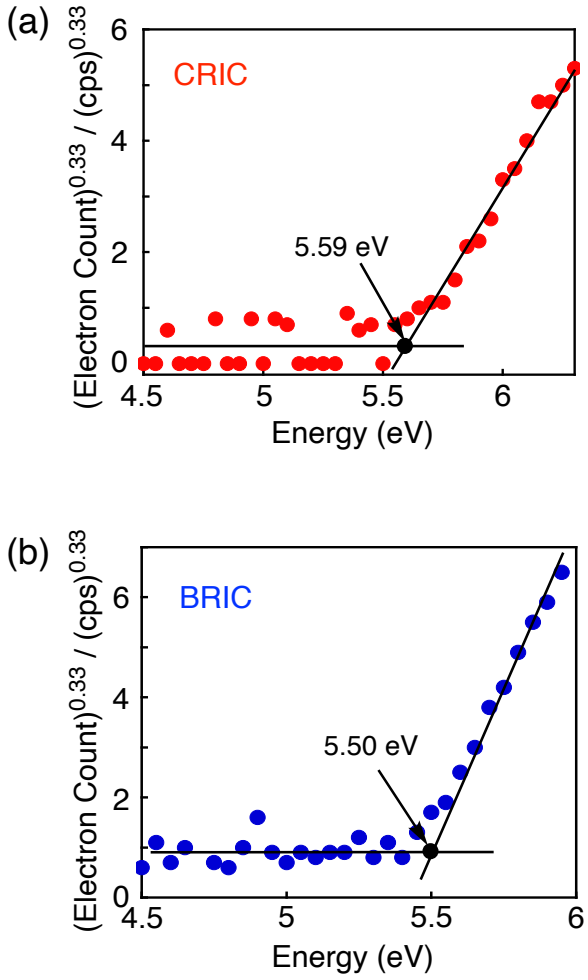

Fig. S21 Photoemission yield spectroscopy in air (PYSA) of (a) CRIC and (d) BRIC films.

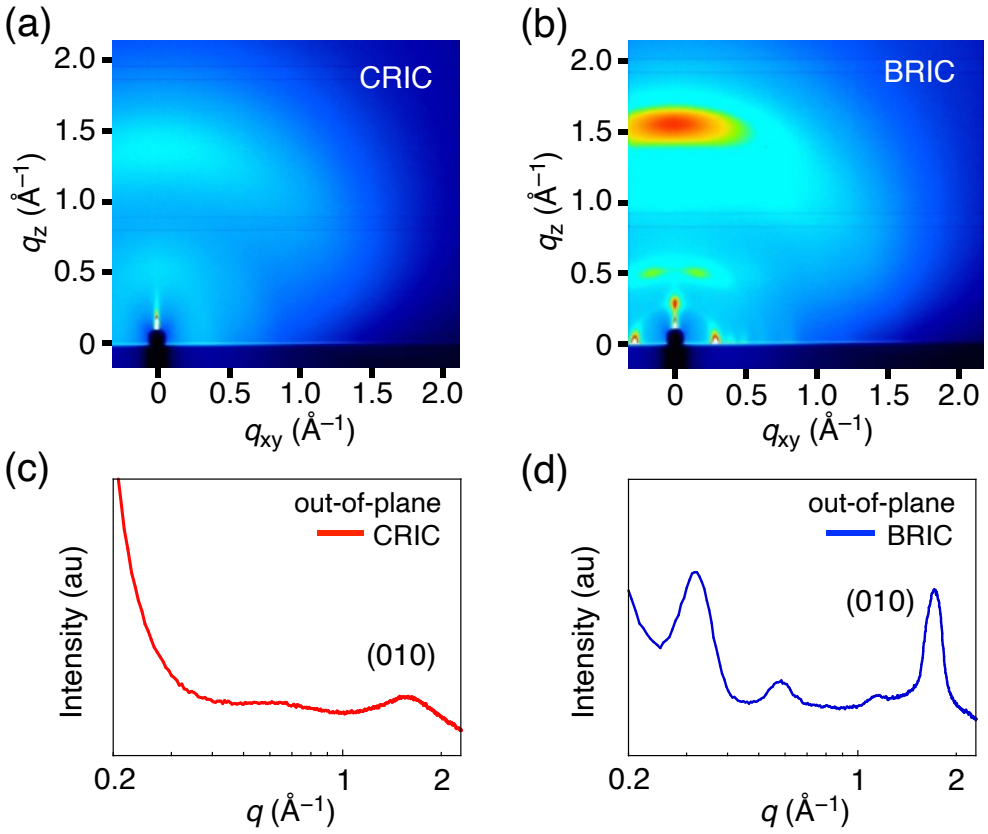

Fig. S22 Two dimensional GIWAXS plots of (a) CRIC and (b) BRIC neat films on glass substrates. Out-of-plane GIWAXS profiles for (c) CRIC and (d) BRIC neat films.

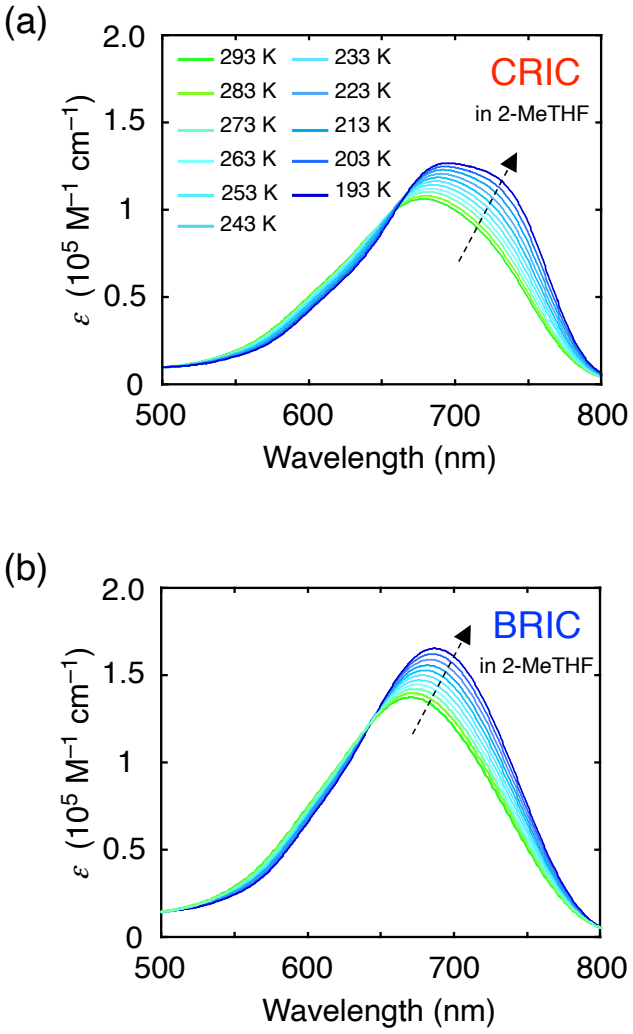

Fig. S23 Absorption spectra of (a) CRIC and (b) BRIC in 2-MeTHF at a concentration of 0.28 mg mL^{-1} for different temperatures upon cooling from 293 to 193 K. Arrows indicate spectral changes.

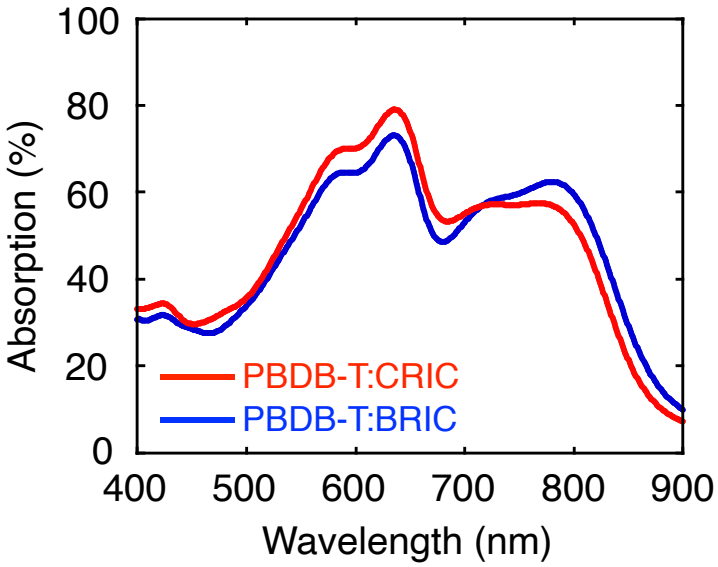

Fig. S24 UV-vis-NIR absorption spectra of PBDB-T:CRIC (red) and PBDB-T:BRIC (blue) on glass substrates. Note here that the total absorption of the ITO/PEDOT:PSS/PBDB-T:NFREA/PDINN/Ag devices are higher than the values in the spectra due to the reflection from the Ag electrode in real devices.

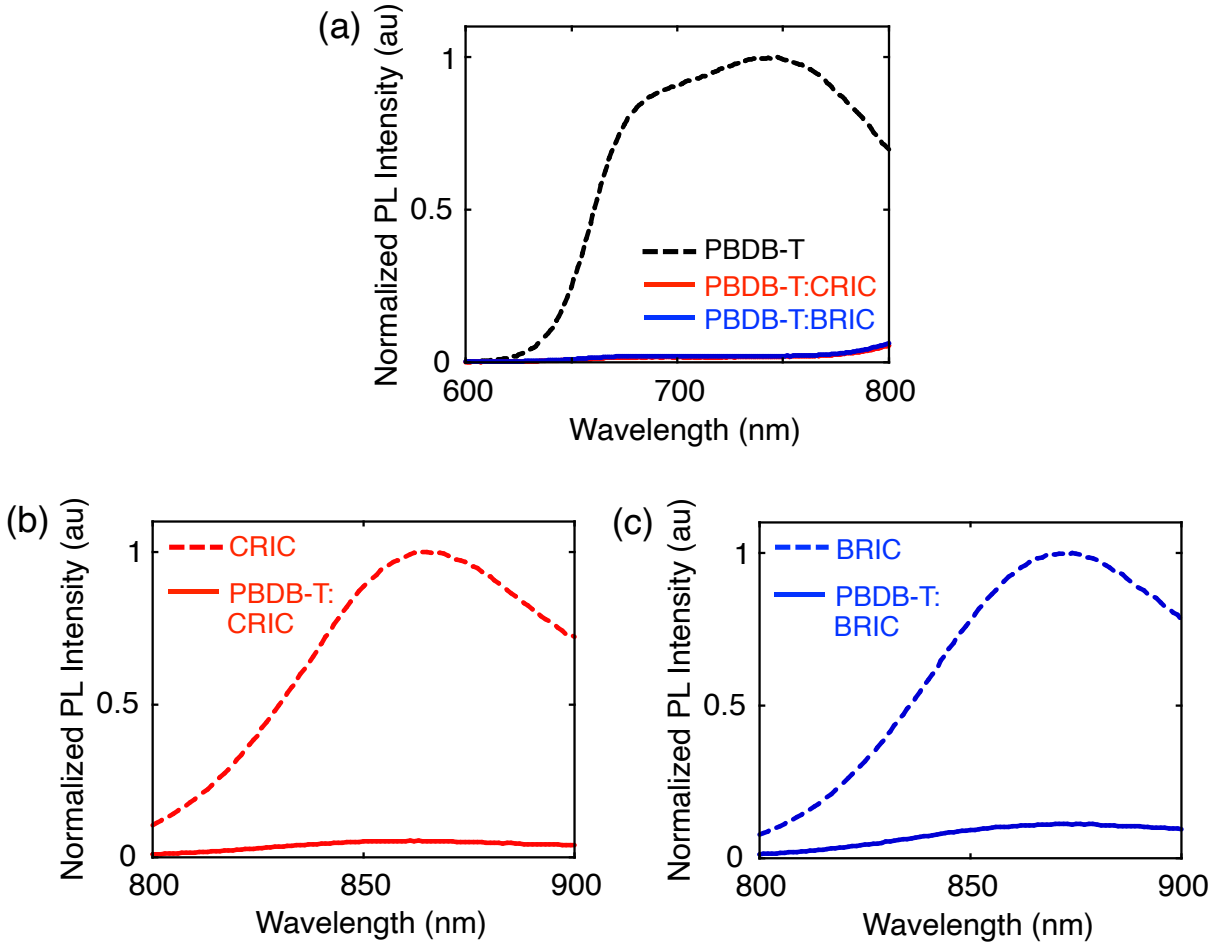

Fig. S25 (a) Photoluminescence spectra of PBDB-T neat film (black dotted) and blend films of PBDB-T with CRIC (red solid) and BRIC (blue solid). The excitation wavelength was 520 nm where PBDB-T was predominantly excited. The emission intensities are normalized by that of the PBDB-T neat film considering the difference in the absorbances of the PBDB-T:NFREA films at the excitation wavelength. (b,c) Photoluminescence spectra of (b) CRIC neat film (red dotted) and PBDB-T:CRIC (red solid) and (c) BRIC neat film (blue dotted) and PBDB-T:BRIC (blue solid). The samples were excited at 710 nm, where the NFREAs were predominantly excited. The emission intensities are normalized by that of the NFREA neat film considering the difference in the absorbances of the PBDB-T:NFREA films at the excitation wavelength.

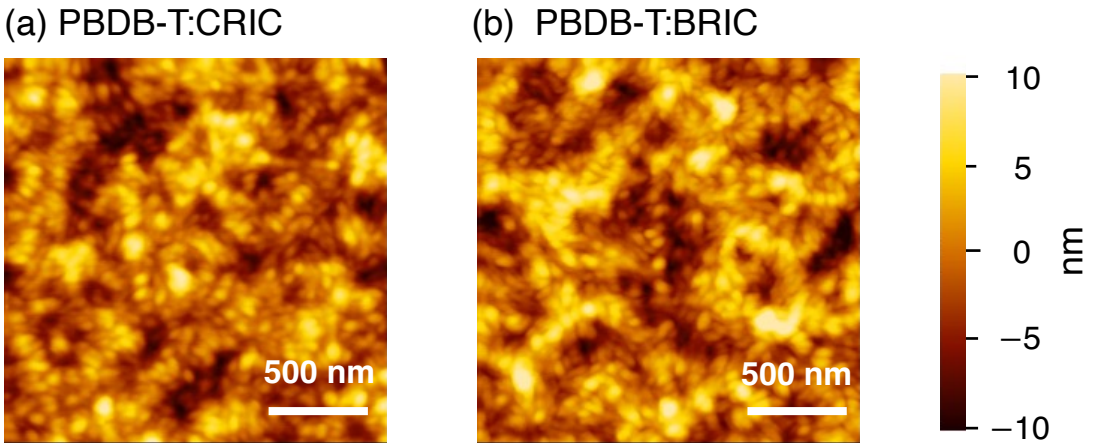

Fig. S26 AFM images of (a) PBDB-T:CRIC and (b) PBDB-T:BRIC on ITO/PEDOT:PSS substrates. The color scale represents the height topography, with bright and dark representing the highest and lowest features, respectively. The root-mean-square (rms) surface roughnesses are (a) 3.36 nm and (b) 3.77 nm.

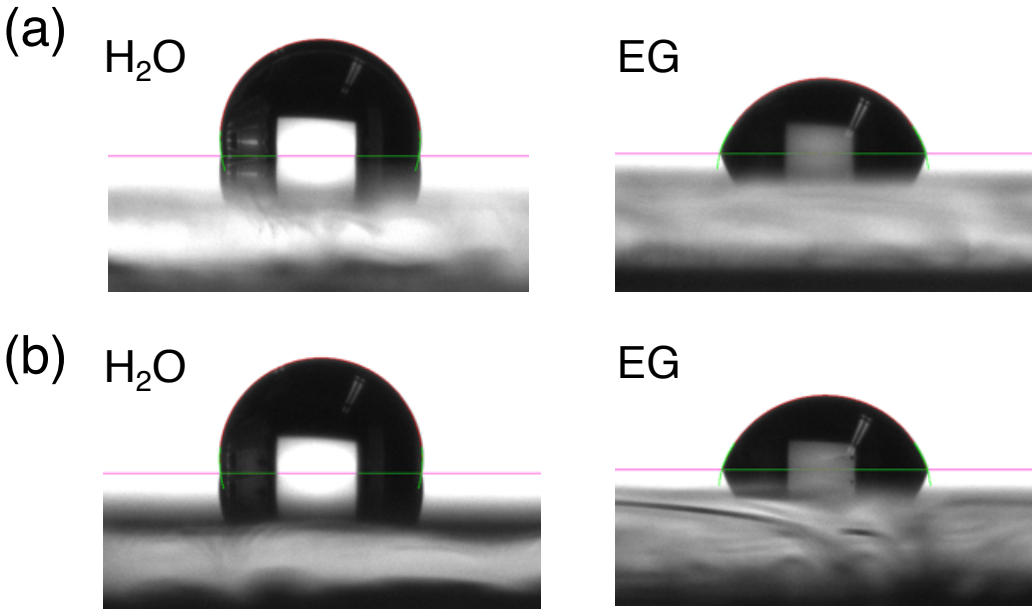

Fig. S27 Contact angle images of (a) CRIC and (b) BRIC neat films with water and ethylene glycol (EG) droplets on top.

Table S1. Contact angles and surface energy parameters.

Material	Contact angle		γ^d (mN m^{-1})	γ^p (mN m^{-1})	γ (mN m^{-1})	$\chi_{\text{donor-acceptor}}$ [b] (K)
	θ_{water} (°)	θ_{oil} (°) [a]				
CRIC	98.85	74.51	14.47	7.66	22.13	0.027
BRIC	97.41	73.66	13.96	8.52	22.49	0.042
PBDB-T	104.3	79.14	15.58	5.02	20.60	/

[a] θ_{oil} represents the contact angle of ethylene glycol. [b] The Flory−Huggins interaction parameters ($\chi_{\text{donor-acceptor}}$) were calculated using the empirical relation:$\chi_{\text{donor-acceptor}} = K(\gamma_{\text{donor}}^{1/2}-\gamma_{\text{acceptor}}^{1/2})^2$, in which K is a constant.

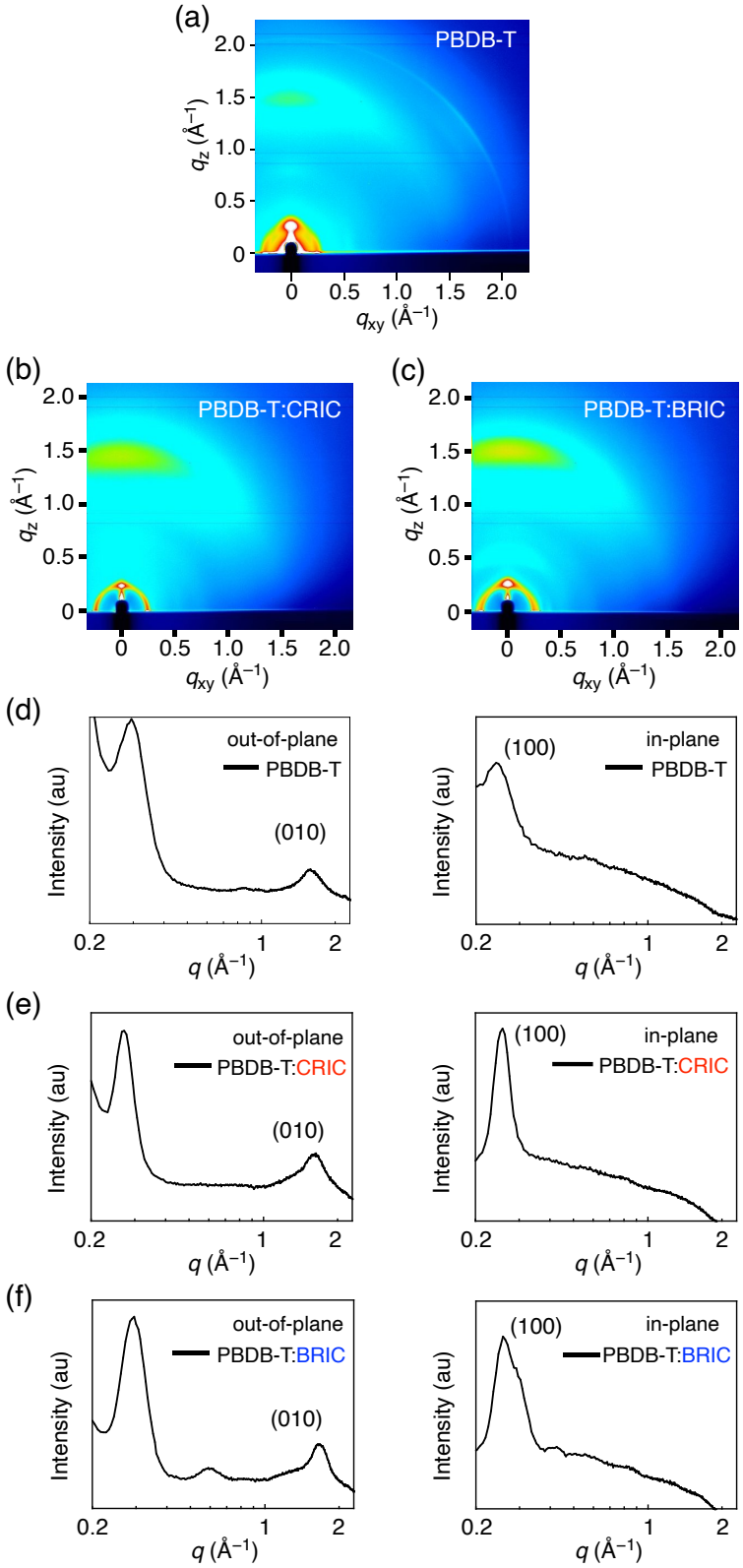

Fig. S28 Two dimensional GIWAXS plots of (a) PBDB-T, (b) PBDB-T:CRIC, and (c) PBDB-T:BRIC. Out-of-plane and in-plane GIWAXS profiles for (d) PBDB-T, (e) PBDB-T:CRIC, and (f) PBDB-T:BRIC.

8. References

[S1] Gaussian 16, Revision B.01, M. J. Frisch, G. W. Trucks, H. B. Schlegel, G. E. Scuseria, M. A. Robb, J. R. Cheeseman, G. Scalmani, V. Barone, G. A. Petersson, H. Nakatsuji, X. Li, M. Caricato, A. V. Marenich, J. Bloino, B. G. Janesko, R. Gomperts, B. Mennucci, H. P. Hratchian, J. V. Ortiz, A. F. Izmaylov, J. L. Sonnenberg, D. Williams-Young, F. Ding, F. Lipparini, F. Egidi, J. Goings, B. Peng, A. Petrone, T. Henderson, D. Ranasinghe, V. G. Zakrzewski, J. Gao, N. Rega, G. Zheng, W. Liang, M. Hada, M. Ehara, K. Toyota, R. Fukuda, J. Hasegawa, M. Ishida, T. Nakajima, Y. Honda, O. Kitao, H. Nakai, T. Vreven, K. Throssell, J. A. Montgomery Jr., J. E. Peralta, F. Ogliaro, M. J. Bearpark, J. J. Heyd, E. N. Brothers, K. N. Kudin, V. N. Staroverov, T. A. Keith, R. Kobayashi, J. Normand, K. Raghavachari, A. P. Rendell, J. C. Burant, S. S. Iyengar, J. Tomasi, M. Cossi, J. M. Millam, M. Klene, C. Adamo, R. Cammi, J. W. Ochterski, R. L. Martin, K. Morokuma, O. Farkas, J. B. Foresman, D. J. Fox, Gaussian, Inc., Wallingford CT, 2016.

[S2] P. Jiang, J. Chen, F. Qin, T. Liu, S. Xiong, W. Wang, C. Xie, X. Lu, Y. Jiang, H. Han and Y. Zhou, *Angew. Chem. Int. Ed*., 2022, **61**, e202208815.

[S3] R.-N. Simizu and N.-R. Demarquette, *J. Appl. Polym. Sci*., 2000, **12**, 1831–1845.

[S4] L. Ma, Y. Cai, S. Li, J. Li, P. Chen, G.-V. Zyryanov, D.-S. Kopchuk, I.-S. Kovalev and Z. Wang, *Anal. Chem.*, 2022, **94**, 14322−14330.

[S5] R. Li, J. Liu, N. Cai, M. Zhang and P. Wang, *J. Phys. Chem. B*, 2010, **114**, 4461–4464.

[S6] T. Umeyama, T. Wada, K. Igarashi, K. Kato, A. Yamakata, T. Takeyama, Y. Sakamoto, Y. Tamai, H. Ohkita, K. Ishida, T. Koganezawa, S. Ohtani, K. Tanaka and H. Imahori, *ACS Appl. Energy Mater*., 2021, **4**, 14022–14033.

[S7] T. Wu, C. Wang, H. Fan, Y. Xia, X. Liu, R. Li, C. Xiao and W. Li, *ACS Appl. Energy Mater.*, 2024, **7**, 1676–1683.

[S8] M. L. Braunger, E. A. Silva, H. Awada, V. J. R. Oliveira, H. Santos Silva, D. Bégué, R. C. Hiorns, C. Lartigau-Dagron, C. A. Olivati, *Polym. Int.*, 2018, **67**, 1028–1034.

[S9] Q. Chai, W. Li, Y. Wu, K. Pei, J. Liu, Z. Geng, H. Tian and W. Zhu, *ACS Appl. Mater. Interfaces*, 2014, **6**, 14621−14630.

[S10] Y. Sun, C. Zhang, B. Dai, B. Lin, H. Yang, X. Zhang, L. Guo and Y. Liu, *J. Polym. Sci. A*, 2015, **53**, 1915−1926.

[S11] S. Ye, S. Chen, S. Li, Y. Pan, X. Xia, W. Fu, L. Zuo, X. Lu, M. Shi and H. Chen, *ChemSusChem*, 2021, **14**, 3599−3606.

[S12] B. He, Y. Meng, X. Lin, Y. Hu, M. Xiao, G. Chen and C. Dai, *Dyes Pigm.*, 2023, **218**, 111478.

[S13] J. Huang, C.-Y. Gao, X.-H. Fan, X. Zhu and L.-M. Yang, *Energy Technol.*, 2022, **10**, 2100912.